ACS OMEGA

http://pubs.acs.org/journal/acsodf

Article

# Titania Nanorods Embedded with 2-Bromo-3-(methylamino)naphthalene-1,4-dione for Dye-Sensitized Solar Cells

Sharad A. Mahadik, Habib M. Pathan,* Sunita Salunke-Gawali,* and Ray J. Butcher

Cite This: *ACS Omega* 2022, 7, 35595−35609

Read Online

ACCESS | Metrics & More | Article Recommendations | Supporting Information

**ABSTRACT:** In a recent study, $TiO_2$ nanorod electrodes were prepared by the hydrothermal approach followed by calcination at various temperatures from 300 to 600 °C. The effects of calcination temperature on the morphological and structural properties were investigated. The novel analogue of aminonaphthoquinone(2R-(*n*-alkylamino)-1,4-naphthoquinone) photosensitizer, viz. BrA1, 2-bromo-3-(methylamino)naphthalene-1,4-dione was synthesized from 2,3-dibromonaphthalene-1,4-dione. X-ray crystallographic data collection and refinement confirm that BrA1 crystallizes in the triclinic space group $P\bar{1}$. After loading BrA1, the photosensitizer on the annealed $TiO_2$ nanorod ($TiO_2$NR) electrodes, the optical properties of the photoanodes showed broadbands in each of the UV and visible regions, which are attributed to the $\pi \rightarrow \pi^*$ and n $\rightarrow \pi^*$ charge-transfer transitions, respectively. The dye-sensitized solar cell (DSSC) system was formed by loading the BrA1 photosensitizer on $TiO_2$NR. The electrochemical impedance spectroscopy (EIS) analyses confirm that calcination temperature improves the charge transportation by lowering the resistance path during the photovoltaic process in $TiO_2$NR (400 °C) photoanode-based DSSCs due to the sufficient photosensitizer adsorption and fast electron injection. Due to the effective light harvesting by the BrA1 photosensitizer and charge transport through the $TiO_2$ nanorod, the power conversion efficiencies (PCE) of the $TiO_2$NR (400 °C/BrA1-based) DSSCs were improved for 2-bromo-3-(methylamino)naphthalene-1,4-dione.

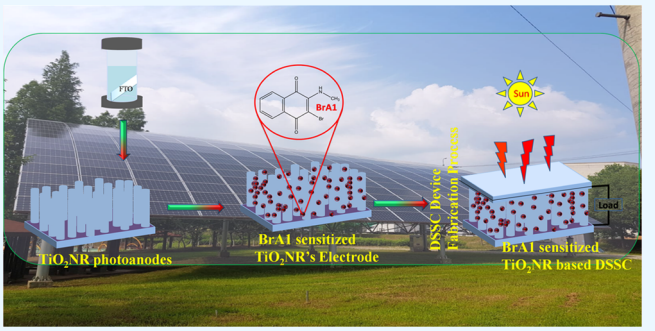


## 1. INTRODUCTION

To meet the rising energy need, the search for new energy sources and easily fabricated photovoltaic devices has recently been of paramount importance. Solar light energy is the clean, most abundant, sustainable, and inexpensive source among the available renewable sources.[1−3] Photovoltaic devices have attracted great interest in achieving efficient solar energy utilization due to their effective solar energy to electrical energy conversion efficiency.[4−7] However, the photovoltaic performance of photovoltaic devices (DSSCs) significantly depends on the properties of the photoanode materials and their structure.[3,5,8,9] Till today, numerous semiconductors (ZnO, $TiO_2$, $Zn_2SnO_4$, and $SnO_2$) have been used as photoanode materials to drive reactions in solar cells.[10−16] Due to its specific properties such as nontoxicity and strong chemical stability, $TiO_2$ is considered one of the capable photocatalyst candidates.[17,18] However, due to the wide band gap (3.0−3.2 eV), $TiO_2$ can absorb only ultraviolet light from the solar spectrum. Thus, out of the total light available from the solar spectrum, $TiO_2$ absorbs only 4−5% incident light, while nearly 43% of the visible light in the solar energy is wasted.[19] Thus, under visible-light irradiation, the overall efficiency of light absorption over $TiO_2$ is limited.[20,21] However, in the case of the $TiO_2$ nanorod photoanodes-based DSSCs, $TiO_2$ acts as a framework to transport the electron photogenerated by light absorption and helps in adsorption of more dye molecules and regeneration.[22] Till today, various attempts have been made to advance $TiO_2$ transport ability to increase DSSC solar energy conversion efficiencies.[23] $TiO_2$ semiconductors with different morphologies of nanorods, nanotubes, spherical, and squares have been synthesized by various sol−gel and hydrothermal approaches.[24−26] This hydrothermal approach led to simple operation conditions to produce $TiO_2$ with different shapes and controlled surface area with porosity. This assists in modification of the surface area, crystal size, and band-gap energy of the $TiO_2$ semiconductor to improve DSSC efficiency.[27] Mathew et al. used the $TiO_2$ electrode, porphyrin photosensitizer (SM 351), with the cobalt (II/III) redox shuttle to form DSSCs that exhibited 13% PCE at 1 sun illumination.[28] Further, Kakiage et al. also reported using the silyl-anchor photosensitizer of ADEKA-1 and the carboxy-

Received: May 23, 2022
Accepted: September 5, 2022
Published: September 27, 2022

anchor group organic photosensitizer LEG4 in DSSCs, and obtained 14.3% power conversion efficiency using $TiO_2$ photoelectrodes and graphene nanoplatelets (GNP) as a counter electrode with the cobalt(II/III) redox shuttle.[29] However, the effects of various parameters such as the photosensitizer's structure, electrolyte, photoanode morphology, and the counter electrode effect on the efficiency of DSSCs have been studied.[30−33] Furthermore, in addition to the reported well-known photosensitizers, organic photosensitizers are expected to have various advantages compared to inorganic photosensitizers.

Generally, these organic photosensitizers are made up of a donor-$\pi$-acceptor (D-$\pi$-A) system. When used to photosensitize the photoanode materials, the acceptor parts are attached to the surface of semiconductors.[34] Therefore, the $Nb_2O_5$ photoanode sensitized with N3 dye showed 2% efficiency,[35] whereas ZnO sensitized with N719 dye exhibited 5% PCE.[36] In this investigation, BrA1 was used as a donor-$\pi$-acceptor (D-$\pi$-A) photosensitizer in the DSSC structures. DSSCs fabricated using aminonaphthoquinone-based photosensitizers, viz. 2-bromo-3-propylamino-1,4-naphthoquinone and 2-bromo-3-butylamino-1,4-naphthoquinone, and mesoporous ZnO photoelectrodes were shown to have an impressive startup PCE of 0.13 and 0.20%, respectively.[37] As reported in the literature, the modifications of photoanode in terms of morphology, doping, and film thickness have significant influences on the PV performance of DSSCs.[38] On the one hand, the photosensitive dyes provide photoelectrons; on the other hand, the bulk of semiconductor materials is only used as a charge transporter.[39] However, due to their nanorod structures, even though the $TiO_2$ nanorod-based electrodes exhibit effective charge transport pathways for the photogenerated electrons in DSSCs, the dye loading in the ZnO-based powder was higher in our previous work due to the nanograin structures,[37] which gave sufficient surface area for light harvesting. However, to improve the dye loading and light absorption, in the near future, we will modify the surface of $TiO_2$NR-based photoanode materials, particularly by loading the $TiO_2$ grains on $TiO_2$ nanorods to improve the dye loading and light absorption simultaneously. Previous literature shows that excessive research has been done on DSSCs; however, in the 1970s, the ZnO-single crystals based on dye-sensitized solar cells[40] showed very poor efficiency due to the monolayer of dye molecules being able to absorb only 1% incident light. Furthermore, progress has been made in improving the efficiency by optimizing various parameters such as the porosity of the electrode, surface area, and optical transparency of the photoelectrode, by designing the sensitizers with functional groups such as −COOH, $-PO_3H_2$, and $-B(OH)_2$.[41−43] In DSSCs, the semiconductor photoanodes are only used as charge transporter and the photoelectrons are provided by photosensitive dyes. Therefore, over the years, many experiments have been carried out on DSSCs to improve their efficiency by developing and studying various organic dyes such as silyl-anchor and carboxy-anchor dyes ruthenium dye, panchromatic black dye, etc.[44,45] Although organic sensitizers have become a good competitor due to their low-cost purification process and ability to tailor the absorption band in the solar spectrum, it is important to recognize the kinetics of photo-excited electrons during DSSC operation.[46] Mainly, the D−$\pi$−A configuration showed better light-harvesting capacity between the visible and far-red regions of the solar spectrum.[47] An organic dye's electrochemical and optical properties are also influenced by intramolecular charge transfer.[48] Therefore, many efforts have been made to engineer the sensitizer (dye) to prohibit charge recombination, reinforce dye regeneration, and cover a broader absorption band in the solar spectrum.[49−51] As the performance of DSSCs has been strongly relying on the molecular structure of the photosensitizer, it is essential to engineer the structures of organic dyes to harvest solar light more efficiently. Consequently, inspired by previous literature, we have synthesized a novel analogue of the aminonaphthoquinone-based photosensitizer, viz. BrA1, 2-bromo-3-(methylamino)naphthalene-1,4-dione (molecular structure of BrA1 and used as a photosensitizer for stable $TiO_2$ photoanodes). BrA1 was used as a donor-$\pi$-acceptor (D-$\pi$-A) photosensitizer in the DSSC structures. Thus, it is expected that further improvement of the power conversion efficiencies of $TiO_2$-based DSSCs can be achieved by forming state-of-the-art devices by combining the hydrothermal syntheses of $TiO_2$ nanorod-based electrode materials with a novel analogue of 2-bromo-3-(methylamino)-naphthalene-1,4-dione as the photosensitizer.

Therefore, inspired by our previous work, herein, we have synthesized a novel analogue of aminonaphthoquinone-based photosensitizer, viz. BrA1, 2-bromo-3-(methylamino)-naphthalene-1,4-dione (molecular structure of BrA1 shown in Figure 1a) for use as a photosensitizer for stable $TiO_2$ photoanodes. After the photosensitizer is adsorbed on the $TiO_2$NR photoanodes, the ligand to metal charge transfer occurs due to titanium (IV) chelation with the amine group. This further leads to the formation of the bidentate complex by adsorption of the amino group with titanium (IV). Additionally, the oxygen and nitrogen atoms of BrA1 are involved in the physical contact with the titanium (Ti) atom of $TiO_2$. Thus, the interface between BrA1 and $TiO_2$ is formed. The possible schematic interfacial contact structures of BrA1 and $TiO_2$ are shown in Figure 1b.

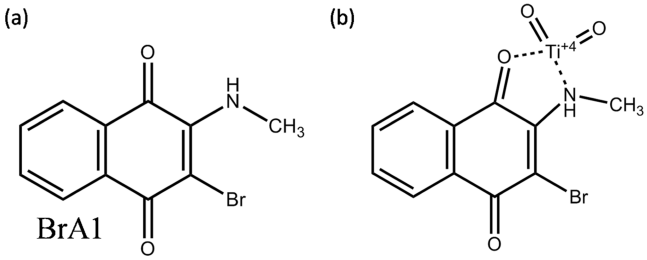


**Figure 1.** (a) Molecular structure of the photosensitizer (2-bromo-3-(methylamino)naphthalene-1,4-dione) and (b) schematic of the interfacial contact structure of BrA1 and $TiO_2$.

Furthermore, $TiO_2$ nanorod ($TiO_2$NR) photoanodes were synthesized by the hydrothermal technique and annealed at different temperatures of 300, 400, 500, and 600 °C for 2 h. Furthermore, the effect of calcination temperatures on the optical, structural, and morphological properties of $TiO_2$NR has been investigated. Then, a DSSC device was developed by loading the BrA1 photosensitizer solution as BrA1 on the $TiO_2$NR-based photoelectrodes in a separate set of experiments. Further, device characteristics in terms of the photocurrent, carrier recombination, and transport times of the fabricated photoanodes ($TiO_2$NR (300 °C)/BrA1, $TiO_2$NR (400 °C)/BrA1, $TiO_2$NR (500 °C)/BrA1, and $TiO_2$NR (600 °C)/BrA1) were investigated in detail. This study would first use BrA1 as a photosensitizer for the $TiO_2$NR


https://doi.org/10.1021/acsomega.2c03208
ACS Omega 2022, 7, 35595−35609

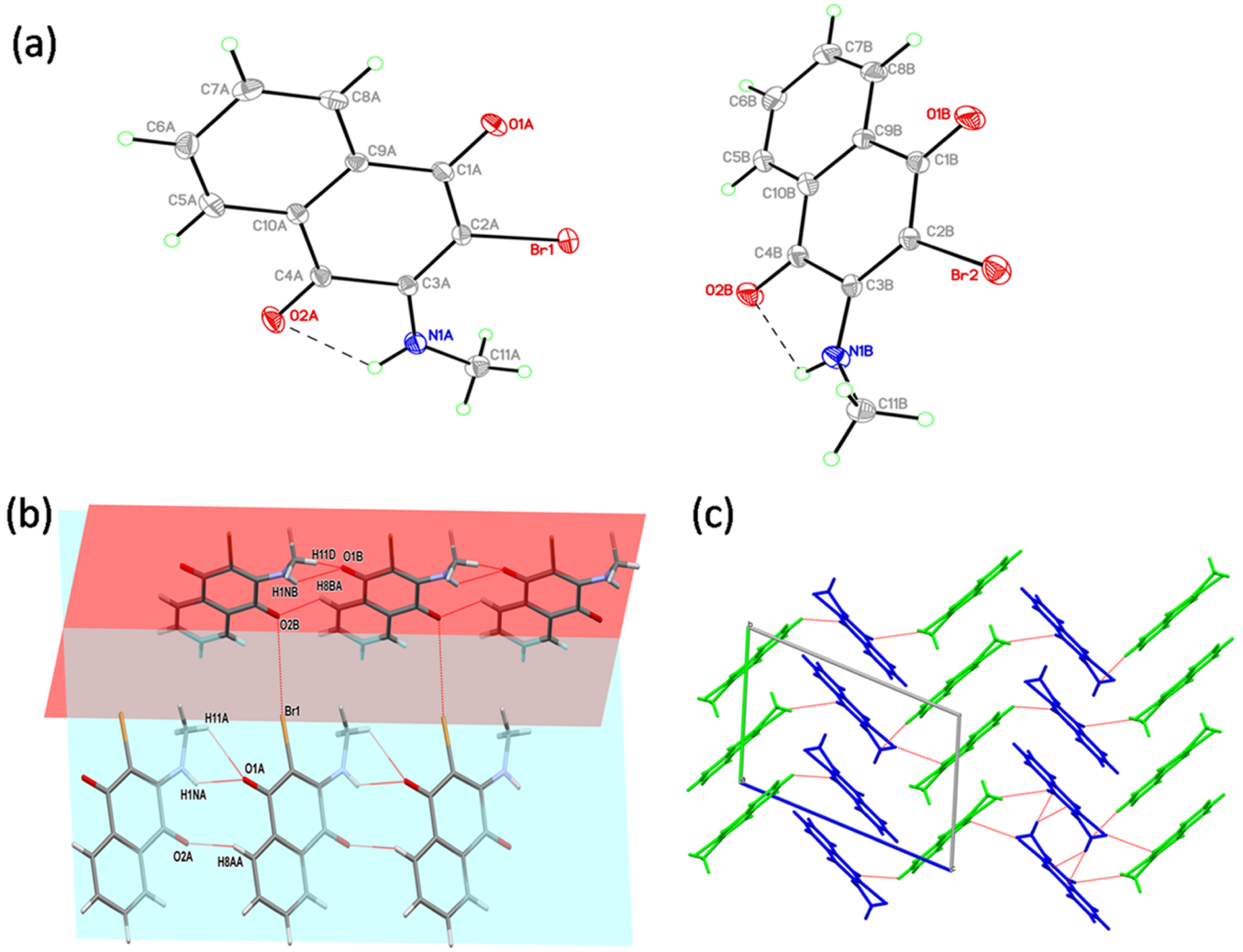


**Figure 2.** (a) ORTEP of BrA1 and (b, c) polymeric chains of asymmetric molecules of BrA1 down the a-axis.

photoanode. Thus, our work will soon open a new approach to using the novel BrA1 photosensitizer for various metal oxide photoanodes' light-harvesting and DSSC photoelectric conversion efficiency.

## 2. EXPERIMENTAL SECTION

**2.1. Materials and Methods.** The materials used, viz. 2-bromo-3-(methylamino)naphthalene-1,4-dione photosensitizers, were synthesized and characterized using the literature-reported procedure and purified by column chromatography with toluene:methanol (9:1) as eluent.[52] 2,3-Dibromonaphthalene-1,4-dione (DBrNQ) and fluorine-doped tin oxide (FTO) having a resistance of 16 Ω/□ (ohms per square) were purchased from Sigma-Aldrich. Methylamine (40%) was purchased from LOBA Chemicals India. Methanol (AR), ethanol (AR), dichloromethane (AR), and toluene (LR) were purchased from Merck Chemicals. Dimethyl sulfoxide (HPLC; Sigma-Aldrich), titanium (IV) butoxide (97%; Sigma-Aldrich), and hydrochloric acid (35−37%; Junsei, Japan) were used as received. Toluene was purified by standard reported methods,[53] and dry methanol was prepared by the literature-reported procedure.[54]

**2.2. Preparation of Photoelectrodes ($TiO_2$ Nanorod Arrays).** *2.2.1. Preparation of $TiO_2$ Nanorod Photoelectrodes and BrA1 Photosensitizer.* Photoelectrodes of $TiO_2$NR semiconductors were prepared on the surface of FTO. F-doped $SnO_2$ has a resistance of 16 Ω/□. Initially, the conducting substrate of the FTO was cleaned with a soap solution for 10-15 min, followed by ultrasonication for 15 min, and then cleaned using double-distilled water (DDW).[55,56] The modified hydrothermal process was used to synthesize the $TiO_2$ nanorods ($TiO_2$ NR) on FTO.[57−59] In the typical synthesis process, 60 mL of 1:1 ratio of DDW and concentrated HCl were mixed under constant stirring for 5 min, adding 1 mL of titanium (IV) butoxide and stirring for 30 min. Finally, the resultant solution was transferred into a Teflon-lined stainless steel autoclave with two FTOs kept in the autoclave. The autoclave was tightly closed and placed in an electric oven at 150 °C for 4 h. After deposition, the $TiO_2$NR photoanodes were washed with DDW and dried at room temperature (27 °C).[60,61] Further, these as-prepared $TiO_2$NR films were annealed at different temperatures such as 300, 400, 500, and 600 °C, respectively, in a box furnace with a 5 °C/min ramp step. Moreover, the BrA1-photosensitized $TiO_2$NR photoelectrodes were prepared via the chemical bath deposition method. Initially, a 0.01 M solution of photosensitizer (BrA1) in methanol was prepared in five separate beakers. Then, one hydrothermally prepared $TiO_2$NR photoanode (300, 400, 500, and 600 °C) was dipped into the sensitizer solution for 72 h at 27 °C under the dark condition.



https://doi.org/10.1021/acsomega.2c03208
ACS Omega 2022, 7, 35595−35609

After 72 h of adsorption of photosensitizers, the photoelectrodes were washed with ethanol for 10 s to remove the unloaded photosensitizer molecules. Finally, the BrA1-photosensitized $TiO_2$NR photoelectrodes were denoted as $TiO_2$NR (300 °C)/BrA1, $TiO_2$NR (400 °C)/BrA1, $TiO_2$NR (500 °C)/BrA1, and $TiO_2$NR (600 °C)/BrA1.

**2.3. Characterization of Photosensitizers and $TiO_2$ Nanorod Array Photoelectrodes.** The morphology of the photoanodes was further analyzed using the JEM-2010 field emission-scanning electron microscopy (FE-SEM) instrument (SUPRA40VP, Germany). The structure and crystallite size of the prepared $TiO_2$NR-based photoelectrodes were calculated using a powder X-ray diffractometer, Bruker D8, with Cu K$\alpha$ radiation source of wavelength ($\lambda$) = 0.154 nm in the angular range of 20−80°. The X-ray tube had a fixed current of 30 mA and a voltage of 40 kV. For X-ray photoelectron spectroscopy (XPS), a Thermo Scientific XPS spectrometer equipped with a monochromatic Al K$\alpha$ X-ray source (h$\upsilon$ = 1486.6 eV) was used to study the elemental composition and valence state of the photoanodes. The UV−visible absorption spectra of the photosensitizer and photoanodes were collected using the Jasco Ultraviolet-Visible spectrophotometer model (V-670). The photosensitizer's cyclic voltammetry (CV) studies were performed using a CH instrument with an electrochemical analyzer (CHI 6054E). Fourier-transform infrared spectroscopy (FT-IR) spectra of the photosensitizer (BrA1) and photosensitizers-loaded photoanodes were recorded in the range 4000−400 $cm^{-1}$ using a BRUKER FT-IR spectrophotometer.

Single-crystal X-ray diffraction data for BrA1 were collected using a D8 Venture PHOTON 100 CMOS diffractometer using graphite-monochromatized Mo K$\alpha$ radiation ($\lambda$ = 0.7107 Å) with exposure/frame = 10 s. The X-ray generator was operated at 50 kV and 30 mA for Mo K$\alpha$ radiation, and at 50 kV and 1 mA for Cu K$\alpha$. An initial set of cell constants and an orientation matrix were calculated from 24 and 60 frames for the Mo and Cu sources. The optimized strategy for the data collection consisted of different $\varphi$ and $\omega$ scans with 0.5° steps of $\varphi/\omega$. The crystal to detector distance was 5.00 cm with 512 × 512 pixels/frame, oscillation/frame = −0.5°, maximum detector swing angle = −30.0°, beam center = (260.2, 252.5), and in-plane spot width = 1.24. Data integration was carried out with a Bruker SAINT program, and empirical absorption correction for intensity data was carried out subsequently by Bruker SADABS. The programs were integrated into the APEX II package.[62] The data was corrected for Lorentz and polarization effect. The structures were solved by the *Direct Method* using SHELX-97.[53] The final refinement of the structure was performed by full-matrix least-squares techniques with anisotropic thermal data for the non-hydrogen atoms on F2. The non-hydrogen atoms were refined anisotropically, while hydrogen atoms were refined at the calculated positions as riding atoms with isotropic displacement parameters. Molecular diagrams were generated using the Mercury program.[63] Geometrical calculations were performed using SHELXTL[64] and PLATON.[65]

## 3. RESULTS AND DISCUSSION

**3.1. Single-Crystal X-ray Diffraction Studies of the BrA1 Photosensitizer.** BrA1 crystallizes in the centrosymmetric triclinic space group $P\bar{1}$. The ORTEP diagram is shown in Figure 2a. The crystal structure data are shown in Table S1 in ESI† and the hydrogen bonding parameters in Table S2 in ESI†. The asymmetric unit's two BrA1 molecules are present in the asymmetric unit; these molecules differ by bond distances (Figure S1 in ESI†) and noncovalent interactions (Figure S2 in ESI†). Molecule A (Figure 2a, atom numbered as A) is in the vicinity of four similar molecules, while molecule B (Figure 2a, atom numbered as B) is connected to six nearest similar molecules. Only asymmetric molecule B shows C−H···$\pi$ interaction (Figure S2 in ESI†). The quinonoid carbonyl distances of both the asymmetric molecules are similar to the oxidized form of naphthoquinone.[52,66−69] Both the asymmetric molecules form a polymeric chain-like structure via *"head to tail"* N−H···O and C−H···O (benzenoid proton) interactions, and methyl of *n*-alkylamino also supports C−H···O interaction. The planes of the polymeric chain of asymmetric molecules make an angle of 88.71° (Figure 2b). Figure 2c shows the intermolecular interaction between the polymeric chains of A and B molecules via Br···O and C−H···O interactions; the C−H···$\pi$ interaction of molecule B is visible. The crystallographic data for BrA1 are shown in Tables S1−S7 in ESI†.

**3.2. Surface Morphology of $TiO_2$NR Photoanodes.** Figure 3 shows the surface and cross-sectional FE-SEM of

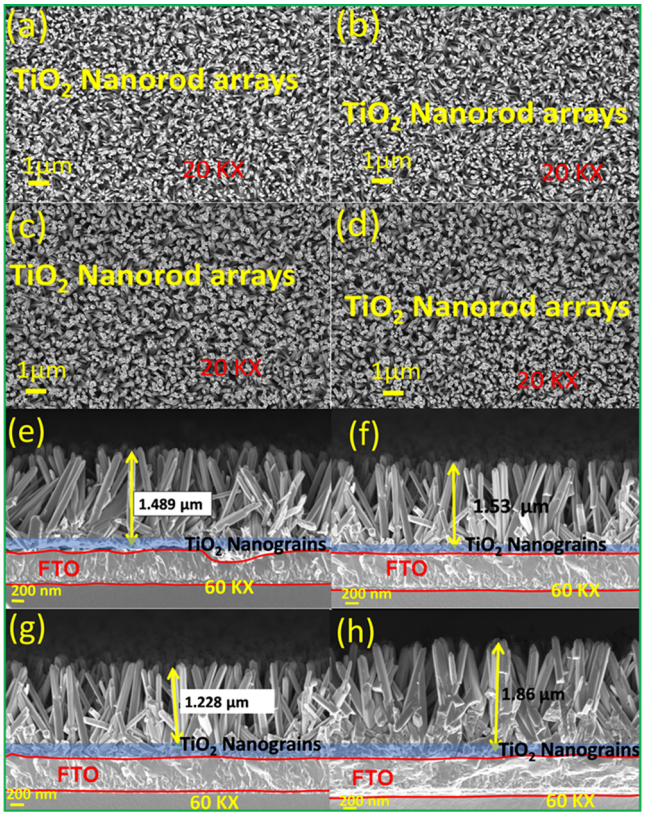


**Figure 3.** Surface FE-SEM images of (a−d) hydrothermally deposited $TiO_2$NR photoanodes; (e−h) cross-section views of the hydrothermally deposited $TiO_2$NR photoanodes.

$TiO_2$NRs grown on the FTO surface by the hydrothermal process and annealed at various temperatures ranging from 300 to 600 °C for 1 h. As shown in Figure 3a−d, the whole surface of FTO is covered with vertically aligned $TiO_2$NRs. The upper faces of the nanorods are round-shaped, and some space is present between two hydrothermally deposited $TiO_2$NR. This porous structure could be helpful during photosensitizer loading and photovoltaic measurements.[70] Additionally, during the DSSC measurements, more electrolyte was inserted into


https://doi.org/10.1021/acsomega.2c03208
ACS Omega 2022, 7, 35595−35609

the porous structure of $TiO_2$NR, and thus, the maximum active surface area of $TiO_2$ can be utilized during the DSSC application.[59] Figure 3e−h shows that the thicknesses of the $TiO_2$NR photoelectrodes ($TiO_2$NR (300 °C), $TiO_2$NR (400 °C), $TiO_2$NR (500 °C), and $TiO_2$NR (600 °C)) are approximately 1.48, 1.53, 1.22, and 1.86 $\mu$m, respectively. Generally, a simple single-step chemistry approach involves hydrothermally synthesized $TiO_2$ nanorods, forming thin $TiO_2$ grains on FTO as seed particles for $TiO_2$ nanorod growth. This thin $TiO_2$NR nanograins layer helps to keep contact between the $TiO_2$NR and the FTO substrate. Also, the interface contact between the $TiO_2$NR and the substrate improves as the calcination temperature increases. After increasing the calcination temperature above 400 °C, a thicker compact optimum $TiO_2$ layer forms between the $TiO_2$NRs and substrate interface. This is due to the nanocrystals gradually crystallizing with the annealing temperature. Further, due to high-temperature annealing, some nanocrystals split and are formed with more compact contact between the $TiO_2$ and FTO interface. The SEM cross-sectional views of the interface between the $TiO_2$ nanorods array and the FTO substrate are shown in Figure 3e−h. Generally, it is expected that the hydrothermally synthesized $TiO_2$ nanorods would involve a simple single-step chemistry approach, which uses small $TiO_2$ grains as seed particles for nanorod growth, as shown in the FTO/$TiO_2$ interface. In this process, the hierarchical non-porous $TiO_2$ spheres serve as scaffolds that provide plenty of conductive tunnels for efficient charge transfer and the subsequent growth of $TiO_2$ nanorods. Further, as the annealing temperature increases to 400 °C, the amorphous nanocrystals gradually crystallize and act as cores, leading to the continuous growth of the $TiO_2$ nanorods. This facilitates the formation of a tamping contact on the surface of FTO, which helps reduce the resistance between FTO and the $TiO_2$ electrode and results in an average thickness of the interconnected nanograins layer of 50−75 nm. However, when the annealing temperature was extended to 500 °C when the nanocrystals gradually crystallized, some of the nanocrystals split and formed with more compact contact between the FTO interface, leading to the continuous transfer of photogenerated charge carriers across the interface. Interestingly, additional growth of the $TiO_2$ nanocrystals was observed at the 600 °C annealing temperature, which enhanced the grain boundary resistance between the grains and decreased the DSSC performance. This continuous growth of nanocrystals occurred at the expense of a thick portion of the nanocrystal with a higher grain boundary resistance, thus resulting in a lower photocurrent. Ghicov et al. indicated that $TiO_2$ nanotubes might collapse at specific heat-treatment conditions, such as high temperatures and long annealing times. Based on the observations from this study, the photocurrent decreased significantly for the $TiO_2$ nanotubes annealed at 600 °C.[71]

**3.3. X-ray Diffraction Analysis of $TiO_2$NR Photoanodes.** Figure 4 shows the XRD peaks of the FTO substrate; hydrothermally deposited $TiO_2$NR's photoanodes annealed at 300, 400, 500, and 600 °C exhibited the diffraction peaks at $2\theta$ = 36.13, 41.2, and 54.31°, which correspond to the tetragonal phase of (rutile) $TiO_2$NRs (reference code 98-002-4277). In contrast, the remaining peaks are assigned to the FTO. The results well agreed with the results obtained by Wu et al.[72] Further, to elucidate the annealing effect on the favored growth orientation of rutile nanorods, the discussion is included based on the available literature.[73,74] To study the influence of

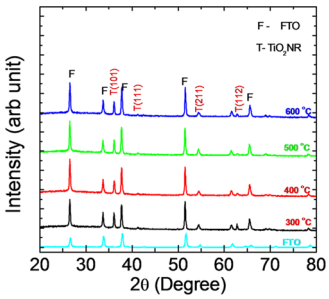


**Figure 4.** The XRD pattern of hydrothermally deposited $TiO_2$NRs grown on the FTO substrate and annealed at 300, 400, 500, and 600 °C.

annealing temperature on the grain size, the crystallite size of the photoanodes annealed at different temperatures was measured. In the present case, it can be seen that among the diffractive reflection peaks (101), (112), and (200) of $TiO_2$NR, (101) is the most prevalent and is used for the crystal size measurements. In the present case, the average crystallite size ($D$) of $TiO_2$NR was calculated using the Debye−Scherrer formula[75]

$$D = \frac{K\lambda}{\beta \cos\theta} \quad (1)$$

where $\lambda$ is the X-ray wavelength in nanometers (nm), $\lambda$ = 0.154 nm is the X-ray wavelength of Cu K$\alpha$, $K$ is the Scherrer constant (0.9), $\beta$ is the full width at half-maximum (FWHM) of the peak, and $\theta$ is the Bragg angle.[76] The (101) peak of the annealed $TiO_2$NRs becomes stronger and sharper with increasing annealing temperature from 300 to 400 °C, indicating better crystallinity. The crystallite sizes of $TiO_2$NR (300 °C), $TiO_2$NR (400 °C), $TiO_2$NR (500 °C), and $TiO_2$NR (600 °C) are 37.69, 34.93, 39.69, and 41.57 nm, respectively. Furthermore, the full width at half-maximum (FWHM) of the (101) peaks of the $TiO_2$NR's photoanodes ($TiO_2$NR (300 °C), $TiO_2$NR (400 °C), $TiO_2$NR (500 °C), and $TiO_2$NR (600 °C)) are shown in Figure S3 in ESI†. However, the crystallinity of $TiO_2$NRs increases at 500 to 600 °C annealing temperature, but the internal surface area of the $TiO_2$NRs might decrease on enhancing the annealing temperature. Similar observations have been reported by Pengn et al. and Zhao et al.[77,78] Thus, in addition to the crystallinity at high-temperature annealing, the photoanodes are significantly affected by other superseding factors such as the internal surface area. Therefore, it can be summarized that the annealing process may not be heating all grains in the sample equally. This led to unequal growth of the grains (few grew in size, whereas others underwent the shrinking process). Thus, during the annealing process, the interface between the growing and shrinking grains undergoes ruptures and detaches the atoms from one another in the same materials. Therefore, the (112) peaks in the $TiO_2$NR's photoanodes annealed at 300 and 600 °C have different intensities than the photoanodes annealed at 400 and 500 °C.[79]

**3.4. XPS of $TiO_2$NR Photoanodes.** To analyze the Ti's elemental composition and valence state in the $TiO_2$NR, $TiO_2$NR (400 °C) photoanodes' and XPS (X-ray photoelectron spectroscopy) analysis was carried out. The survey scan XPS spectra (Figure 5a) of $TiO_2$-based photoanodes indicate the binding energy peaks at 458.4, 565.4, 529.4, and 284.6 eV, respectively, showing that the Ti, O, and C elements


https://doi.org/10.1021/acsomega.2c03208
ACS Omega 2022, 7, 35595−35609

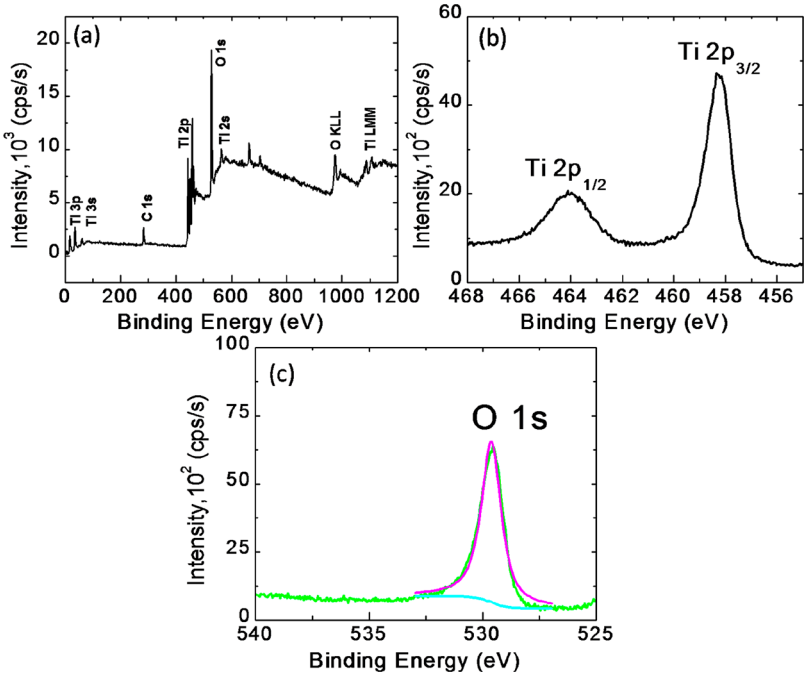


**Figure 5.** (a) X-ray photoelectron spectroscopy (XPS) spectra of hydrothermally deposited $TiO_2$NR (400 °C) photoanode; (b, c) high-resolution XPS spectra of Ti 2p and O 1s, respectively.

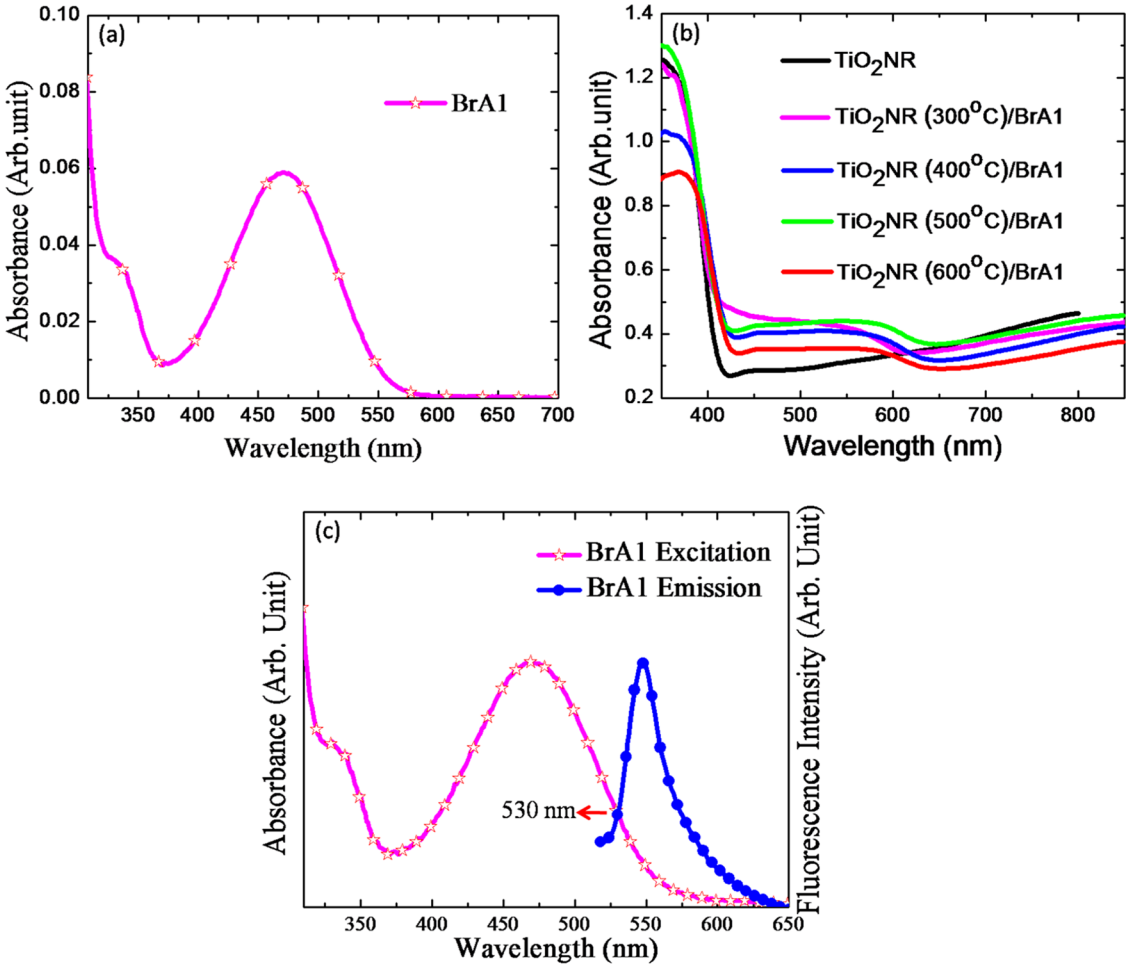


**Figure 6.** UV−visible spectra of (a) BrA1 photosensitizer, (b) unloaded $TiO_2$ and $TiO_2$NR (300 °C)/BrA1, $TiO_2$NR (400 °C)/BrA1, $TiO_2$NR (500 °C)/BrA1, and $TiO_2$NR (600 °C)/BrA1, and (c) excitation and emission spectra of the BrA1 photosensitizer.



https://doi.org/10.1021/acsomega.2c03208
ACS Omega 2022, 7, 35595−35609

are obtained in the film predominantly. The carbon element may be identified by the "C 1s" peak, the carbon element from the organic residue precursors, or the measured environment that was not removed entirely during the hydrothermal process.[80] Figure 5b,c indicates the high-resolution XPS spectra of Ti 2p and O 1s, respectively, for $TiO_2$NR photoanodes. The two strong peaks at around 465.2 and 459.5 eV can be attributed to Ti $2p_{1/2}$ and Ti $2p_{3/2}$, respectively.[60] The calculated binding energy difference between the Ti 2p doublet (Ti $2p_{3/2}$ and Ti $2p_{1/2}$) peaks was 5.7 eV, compatible with the binding energy separation observed for stoichiometric $TiO_2$.[81] The broad O 1s peak, located at about 530.8 eV, is associated with the lattice oxygen of the $TiO_2$NR.[82] This suggests the prepared photoanode is of pure $TiO_2$.

**3.5. UV-Visible Absorption Spectra Photosensitizers (BrA1) and Photoanodes ($TiO_2$NR (300 °C)/BrA1, $TiO_2$NR (400 °C)/BrA1, $TiO_2$NR (500 °C)/BrA1, and $TiO_2$NR (600 °C)/BrA1).** Figure 6a depicts the UV−visible spectra of a 1 $\mu$M concentrated solution of the photosensitizer (BrA1). As shown in Figure 6a, the naphthoquinone exhibits the bands in the UV region at 282 and 330 nm, assigned to the ($\pi \rightarrow \pi^*$) electronic transition. Additionally, the broadband in the visible region was observed at 471 nm due to the weak n $\rightarrow \pi^*$ transition or the charge transfer transition. The electron-donating effect of the substituted amino group shows the charge transfer band in BrA1. The delocalization of the electron lone pair of nitrogen requires its orthogonality in the plane of naphthoquinone. The nature of amines affects their basicity, which affects the extent of the bathochromic shift.[52] This absorption is a typical characteristic of amino-substituted quinone.[83] Generally, it is seen that the charge transfer transition in the visible region is due to the electron-donating effect of the substituted amine in BrA1.[52] The absorption spectra of BrA1 do not depend on the number of polymer-like chains. The absorbance spectra of one- and two-molecule chains were observed at nearly the same wavelength.[52,84] The polymer-like chains are observed via hydrogen bonding of the BrA1 photosensitizer molecules in solid states. The absorption spectra will not affect even though this bonding exists in the solution.[85] Further, Figure 6b indicates the UV−visible spectra of the unloaded $TiO_2$NR and photosensitizer-loaded $TiO_2$NR photoanodes ($TiO_2$NR (300 °C)/BrA1, $TiO_2$NR (400 °C)/BrA1, $TiO_2$NR (500 °C)/BrA1, and $TiO_2$NR (600 °C)/BrA1). The bathochromic shifts in the photosensitizers loaded on photoanodes ($TiO_2$NR (300 °C)/BrA1, $TiO_2$NR (400 °C)/BrA1, $TiO_2$NR (500 °C)/BrA1, and $TiO_2$NR (600 °C)/BrA1) compared to the band of photosensitizer BrA1 are presented in Figure 6, and the corresponding values are shown in Table 1. There is negligible change in diameters are observed to $TiO_2$ nanorods with increase in temperature. Therefore, the absorbance is increased in the $TiO_2$NR 300 °C/BrA1, $TiO_2$NR 400 °C/BrA1, $TiO_2$NR 500 °C/BrA1, and $TiO_2$NR 600 °C/BrA1 photoanodes than the $TiO_2$ bare samples in 400−550 nm region. However, the decrease in the absorption of $TiO_2$ in annealed photoanodes might be due to disordered surfaces and the bulk of nanorods (defects in as-synthesized $TiO_2$NR). The same effect has been reported in the literature.[86,87] It seems that the absorption depends on the dye absorption and the packing density of the nanorods. Therefore, to quantify the $TiO_2$NR's packing density, we calculated the area in each SEM image. We counted several nanorods at two different places, considering the 1 mM area of the SEM image of each sample, and averaged the values. Figure 3e−h shows the cross-sectional views of the nanorod films; the packing density of the array is different for $TiO_2$NR 300 °C/BrA1, $TiO_2$NR 400 °C/BrA1, $TiO_2$NR 500 °C/BrA1, and $TiO_2$NR 600 °C/BrA1 photoanodes. This causes the different absorption in the UV−visible absorption measurements; the $TiO_2$NR 400 °C/BrA1 and $TiO_2$NR 600 °C/BrA1 photoanodes exhibit a lower absorption, with the lowest packing density, whereas for $TiO_2$NR 300 °C/BrA1 and $TiO_2$NR 500 °C/BrA1, with an increase in the amount of packing density, the absorption becomes elevated. The increased packing density helps improve the interfacial contact with BrA1 and further increases the absorption. Further, as reported previously, in 2-(ethylamino)naphthalene-1,4-dione (LH-2) to 2-(hexylamino)naphthalene-1,4-dione (LH6) and 2-(octylamino)naphthalene-1,4-dione (LH8) series, the highest occupied molecular orbital (HOMO) electron density is distributed over the quinone ring and the adjacent nitrogen atom connected with the aliphatic chain and quinone ring. The lowest unoccupied molecular orbital (LUMO) electron density is distributed over the benzenoid ring (naphthalene-1,4-dione ring).[88] Similarly, the electron density distribution occurs in the HOMO and LUMO of the BrA1 photosensitizer. Therefore, to study the HOMO and LUMO energy gap, the intersection of the excitation and emission spectra of the BrA1 photosensitizer are shown in Figure 6c. The HOMO-LUMO energy gap was calculated by using the following formula[89]

$$E = h \times f = \frac{h \times c}{\lambda} = \frac{1240}{\lambda} \quad (2)$$

where $E$ is the optical band gap in eV, $h$ represents the Planck's constant, $\lambda$ represents the intersection of the excitation and emission spectra in nm, and $c$ is the speed of the light. The HOMO-LUMO energy difference is between the vibrationally relaxed ground state and excited state and is denoted by $E_{0\text{-}0}$.[90,91] The $E_{0\text{-}0}$ of the BrA1 photosensitizer is calculated from the intersection of the absorbance and emission spectra of the BrA1 photosensitizer and is equal to 2.33 eV.

**3.6. Electrochemical Investigation Using Cyclic Voltammetry.** Cyclic voltammetry (CV) is one of the outstanding techniques for studying compounds. The cyclic voltammogram of the BrA1 photosensitizer is shown in Figure 7a. The HOMO-LUMO energy difference ($E_{0\text{-}0}$), and HOMO and LUMO energy levels have been calculated using UV−visible, fluorescence spectroscopy, and CV, respectively. The HOMO-LUMO energy difference ($E_{0\text{-}0}$) of the BrA1 photosensitizer is 2.33 eV (Figure 6c). The LUMO can be calculated from the first reduction potential (onset of the first reaction peak) obtained from Figure 7a. Further, the BrA1 photosensitizer reduction peak was specified using CV analysis, and the LUMO was calculated by the formula[92,93]

**Table 1. UV-Visible Data of the Photosensitizer and Photoanodes**

| photosensitizers/ photoanode | UV region (nm) ($\pi \rightarrow \pi^*$) transition | visible region (nm) (n $\rightarrow \pi^*$) transition |
|---|---|---|
| BrA1 | 330 | 471 |
| $TiO_2$NR | 345 | |
| $TiO_2$NR (300 °C)/BrA1 | 361 | 507 |
| $TiO_2$NR (400 °C)/BrA1 | 348 | 507 |
| $TiO_2$NR (500 °C)/BrA1 | 353 | 507 |
| $TiO_2$NR (600 °C)/BrA1 | 366 | 507 |



https://doi.org/10.1021/acsomega.2c03208
ACS Omega 2022, 7, 35595−35609

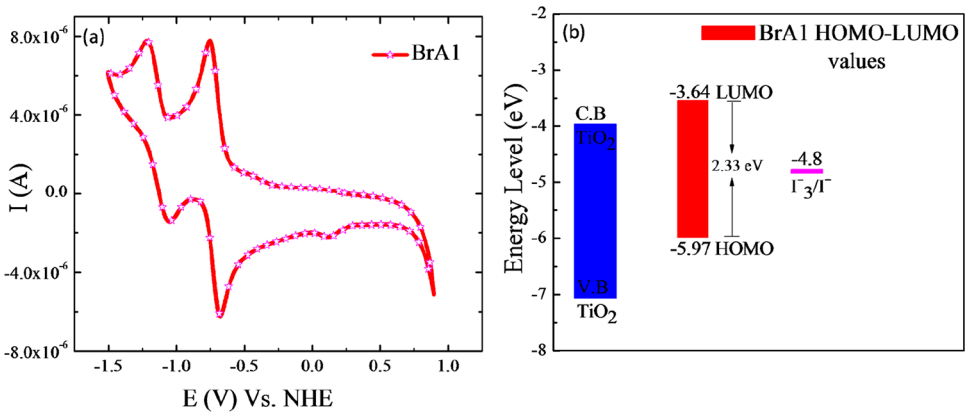


**Figure 7.** Cyclic voltammetry spectra of (a) BrA1 photosensitizer, and (b) energy diagram of the conduction band edge of $TiO_2$ with the HOMO-LUMO values of the BrA1 photosensitizer.

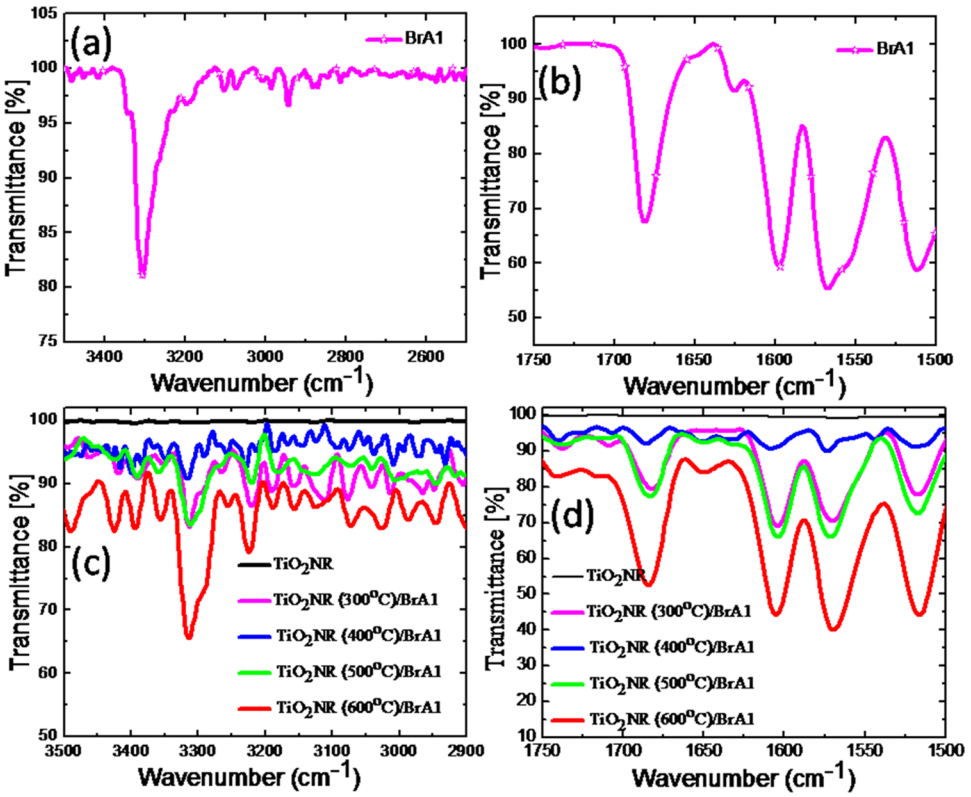


**Figure 8.** (a, b) FT-IR of the photosensitizer (BrA1) and (c, d) FT-IR of photosensitizer-loaded $TiO_2$NR photoelectrodes.

$$E_{LUMO} = -E_{reduction\ onset} - E_{1/2}\left(\frac{FC}{FC^+}\right) - IP(FC)eV \quad (3)$$

$$E_{LUMO} = -E_{reduction\ onset} - IP(FC)eV \quad (4)$$

where IP(FC) is the standard internal redox of the system and $FC/FC^+$ is the Ferrocene/Ferrocenium couple. The $E_{LUMO}$ of the BrA1 photosensitizer is −3.64 eV, and $E_{HOMO}$ is −5.97 eV. The $E_{HOMO}$ was calculated from $E_{LUMO}$ and $E_{0\text{-}0}$ values. Figure 7b shows the energy-level diagram of the conduction band edge of $TiO_2$ with HOMO-LUMO values of the BrA1 photosensitizer. The conduction band of $TiO_2$NR is below the LUMO level of the BrA1 photosensitizer. $TiO_2$NR (400 °C)/BrA1 shows a higher $V_{oc}$, as shown in Table 3. The $TiO_2$NR (400 °C)/BrA1 shows a slower recombination of higher $V_{oc}$. However, as the temperature increases above 400 °C, the $V_{oc}$ value of the $TiO_2$NR-based photoanodes is decreased again. Figure 7b shows that the maximum voltage is the difference between the redox potential of the electrolyte and the Fermi level of $TiO_2$NR. The latter is changed with change in temperature and forms a new Fermi level, i.e., quasi-Fermi level.[94] Therefore, due to the change in the Fermi level of $TiO_2$NR at 400 °C, there is a change in $V_{oc}$.

**3.7. FT-IR Analysis of Photosensitizers and Photoanodes.** To evaluate the photosensitizer (BrA1)/$TiO_2$NR interaction, Fourier-transform infrared (FT-IR) measurements were performed on BrA1 and $TiO_2$NR-based photoanodes ($TiO_2$NR (300 °C)/BrA1, $TiO_2$NR (400 °C)/BrA1, $TiO_2$NR (500 °C)/BrA1, and $TiO_2$NR (600 °C)/BrA1), respectively. Figure 8a,b shows the FT-IR spectra of BrA1, and Figure 8c,d presents the FT-IR of $TiO_2$NR photoanodes ($TiO_2$NR (300 °C)/BrA1, $TiO_2$NR (400 °C)/BrA1, $TiO_2$NR (500 °C)/


https://doi.org/10.1021/acsomega.2c03208
ACS Omega 2022, 7, 35595−35609

BrA1, and $TiO_2$NR (600 °C)/BrA1) in the range 3500−2900 $cm^{-1}$ and 1750−1500 $cm^{-1}$, respectively. Furthermore, for comparison, the FT-IR band frequencies of photosensitizers and photoelectrodes are well summarized in Table 2. It is

**Table 2. FT-IR Band Frequencies of the Photosensitizer and Photoelectrodes**

| photosensitizers/ photoanode | $\nu_{N-H}$ band frequencies ($cm^{-1}$) | $\nu_{C=O}$ band frequencies (cm) | $\nu_{C-N}$ band frequencies ($cm^{-1}$) |
|---|---|---|---|
| BrA1 | 3305 | 1680 | 1596 |
| $TiO_2$NR (300 °C)/BrA1 | 3313 | 1682 | 1604 |
| $TiO_2$NR (400 °C)/BrA1 | 3316 | 1685 | 1608 |
| $TiO_2$NR (500 °C)/BrA1 | 3311 | 1683 | 1603 |
| $TiO_2$NR (600 °C)/BrA1 | 3314 | 1684 | 1604 |

observed that the $\nu_{N-H}$ band of photosensitizer BrA1 (3305 $cm^{-1}$) was increased by 8, 11, 6, and 9 $cm^{-1}$ in their photoanodes ($TiO_2$NR (300 °C)/BrA1, $TiO_2$NR (400 °C)/BrA1, $TiO_2$NR (500 °C)/BrA1, and $TiO_2$NR (600 °C)/BrA1), respectively. On the other hand, the $\nu_{C=O}$ frequencies of photosensitizers observed at 1680 $cm^{-1}$ (BrA1) are shifted to higher wavenumbers (bathochromic shift) by 2, 5, 3, and 4 $cm^{-1}$, respectively, in $TiO_2$NR (300 °C)/BrA1, $TiO_2$NR (400 °C)/BrA1, $TiO_2$NR (500 °C)/BrA1, and $TiO_2$NR (600 °C)/BrA1 with the annealing temperature. The BrA1 photosensitizer anchoring site is attached to $TiO_2$NR through $\nu_{N-H}$ and $\nu_{C=O}$ bonding. The BrA1 photosensitizer shows $\nu_{N-H}$ and $\nu_{C=O}$ frequencies at 3305 and 1680 $cm^{-1}$, respectively, whereas the smaller crystallite size and defect-free $TiO_2$NR (400 °C) photoanode surface help form the attachment of photosensitizer through $\nu_{N-H}$ and $\nu_{C=O}$. The cause of this blue shift might be the presence and interaction of different surface-active sites of $TiO_2$ with a photosensitizer.[91] Thus, as explained earlier, the crystallite size of the $TiO_2$NR (400 °C) photoanode is smaller than that of other photoanodes. The absorption spectra shifted from lower to higher frequencies as the particle size decreased.[95] However, the $\nu_{C-N}$ frequency observed at 1596 $cm^{-1}$ (BrA1) is increased by 8, 12, 7, and 8 $cm^{-1}$, respectively, in $TiO_2$NR (300 °C)/BrA1, $TiO_2$NR (400 °C)/BrA1, $TiO_2$NR (500 °C)/BrA1, and $TiO_2$NR (600 °C)/BrA1. Thus, the shift in the observed frequency in BrA1-loaded $TiO_2$NR suggests the strong interaction between the photosensitizer and base photoanodes, which helps provide a channel for the transfer of electrons in the DSSC system.

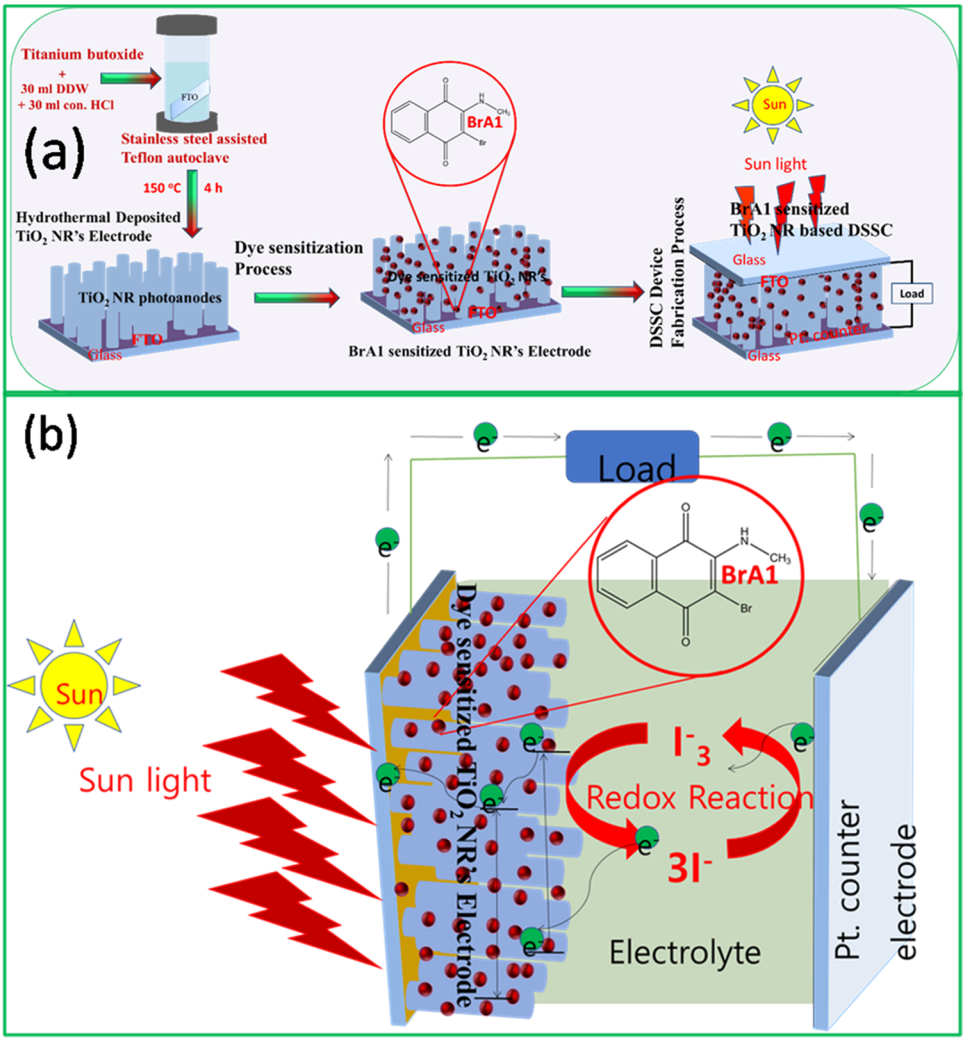


**Figure 9.** (a) Experimental scheme of BrA1-photosensitized $TiO_2$NR-based DSSC and (b) schematic representation for photovoltaic conversion mechanism of $TiO_2$NR (400 °C)/BrA1-based DSSC.



https://doi.org/10.1021/acsomega.2c03208
ACS Omega 2022, 7, 35595−35609

**3.8. Photovoltaic Performance.** *3.8.1. $TiO_2$NR/BrA1 for the Dye-Sensitized Solar Cell (DSSC).* The DSSC was fabricated with crucial parameters such as working electrodes (BrA1-sensitized $TiO_2$NR photoanode). A polyiodide solution (mixture of 0.5 M tetra-*n*-propylammonium iodide ($(CH_3CH_2CH_2)_4NI$) and 0.05 M iodine ($I_2$) in an ethylene carbonate:acetonitrile mixture of solvents in 80:20 proportion) was used as the electrolyte[96] and a Pt electrode was used as the counter electrode.[96] A spacer made up of four layers of cello tape (thickness ∼ 40 $\mu$m) was used between the working electrodes (0.25 $cm^2$ active cell area). The aminonaphthoquinone BrA1 photosensitizer-loaded photoanodes were sandwiched with the counter electrode (Pt electrode). The polyiodide electrolyte was inserted between the working and counter electrodes; simultaneously, care was taken to avoid air bubbles inside the solar cell assembly. This prepared device was further used for photovoltaic measurement. The DSSC components and the experimental scheme of the BrA1-photosensitized $TiO_2$NR-based DSSC are shown in Figure 9a. The photocurrent density voltage ($J-V$) characteristic curves of the DSSCs were measured using a Keithley 2400 source meter and solar simulator (ENLITECH model SS-F5-3A) under the incident light intensity of 100 mW $cm^{-2}$. Generally, in DSSC, EIS measurements are performed under illumination at the voltage corresponding to open-circuit conditions.[97,98] Electrochemical impedance spectroscopy (EIS) was measured using a potentiostat (Vertex IVIUM Technologies Netherlands). The measurements were carried out at an applied potential of −0.5 V with 0.01 V amplitude over a frequency range of 1 Hz−1000 kHz under illumination with an intensity of light of 100 mW $cm^{-2}$. All of the EIS spectra were fitted using ZView software.

The schematic picture of the charge transfer mechanism in a BrA1-sensitized $TiO_2$NR dye-sensitized solar cell is shown in Figure 9b. BrA1 shows the lower energy absorption assigned in the visible region at 471 nm, the charge transfer transition, and the n → $\pi^*$ transition. The charge transfer band indicates the electron-donating effect of the amine group in BrA1.[52] Therefore, in the DSSC fabrication using the BrA1-loaded $TiO_2$NR photoanodes, in addition to $TiO_2$NR itself, the BrA1 absorbs the light and readily donates the electrons to the conduction band of the $TiO_2$NR photoanode. Under light irradiation, the BrA1 dye in the $TiO_2$NR (400 °C)/BrA1-based DSSC absorbs photons equal to or more than the HOMO-LUMO band-gap energy, and electrons are excited from HOMO to LUMO state (Dye*).[99] Further, the photogenerated electrons in the LUMO state of the photosensitizer are excited up into the conduction band of $TiO_2$NR. Some photogenerated electrons revert to the ground state of the BrA1 photosensitizer, and some recombine with the $I_3^-$ in the electrolyte.[100] However, most of the photoelectrons reach the interface of $TiO_2$NR and FTO via $TiO_2$NR channels.

Further, due to the optimum $TiO_2$ compact layer, the photogenerated electrons are easily collected at the current collector and transferred to the platinum counter electrode and the electrolyte. A $TiO_2$ compact layer between $TiO_2$NR and FTO reduces the photoelectrons recombination process in the bulk of $TiO_2$ and the FTO interface and prolongs the electron's lifetime.[79] At the same time, the photogenerated electrons collected at the counter electrode help to prevent the oxidized dye from decomposing and speed up the circulation of the electrons in the DSSC. In addition, the absorption of dye molecules on the $TiO_2$NR surface leads to improved light-harvesting capability. Hence, the significant improvement in the $J_{sc}$ of the BrA1-loaded $TiO_2$NR DSSC ($TiO_2$NR 400 °C)/BrA1 is the synergistic effect of light absorption by BrA1 and effective charge transfer by $TiO_2$NR.

The $J-V$ curves of the $TiO_2$NR (300 °C)/BrA1, $TiO_2$NR (400 °C)/BrA1, $TiO_2$NR (500 °C)/BrA1, and $TiO_2$NR (600 °C)/BrA1 photoanodes-based DSSC are shown in Figure 10.

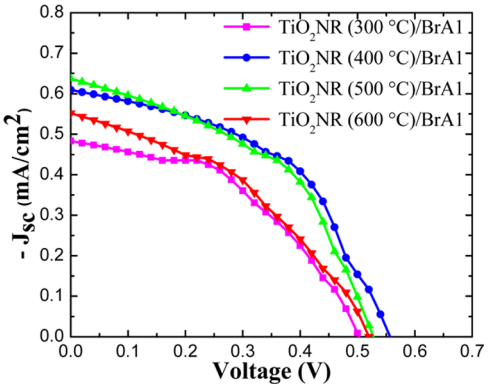


**Figure 10.** $J-V$ characteristic curve of DSSCs based on $TiO_2$NR photoelectrodes annealed at 300, 400, 500, and 600 °C.

The $J-V$ curves of the DSSC device prepared using $TiO_2$NR (400 °C) without the photosensitizer are shown in Figure S4 in ESI†. The $J_{sc}$ and $V_{oc}$ of the $TiO_2$NR (400 °C) without the photosensitizer are nearly equal to zero. During the DSSC photovoltaic analyses, the device was illuminated with 100 mW $cm^{-2}$ (AM 1.5) light intensity. A polyiodide solution was used as the electrolyte. The DSSC parameters of $TiO_2$NR/BrA1 photoanodes such as open-circuit voltage ($V_{oc}$) V, short-circuit photocurrent density ($J_{sc}$) mA/$cm^2$, fill factor (FF), and efficiency ($\eta$) % were calculated and are summarized in Table 3. It is observed that the $J_{sc}$ value for $TiO_2$NR (500 °C)/BrA1

**Table 3. Photovoltaic Performance of BrA1-Sensitized $TiO_2$NR Photoelectrodes at Different Annealed Temperatures**

| photosensitizers/samples | $V_{oc}$ (V) | $J_{sc}$ (mA/$cm^2$) | fill factor | efficiency ($\eta$) % |
|---|---|---|---|---|
| $TiO_2$NR (300 °C)/BrA1 | 0.50 | 0.48 | 44 | 0.10 |
| $TiO_2$NR (400 °C)/BrA1 | 0.55 | 0.60 | 48 | 0.16 |
| $TiO_2$NR (500 °C)/BrA1 | 0.52 | 0.63 | 46 | 0.15 |
| $TiO_2$NR (600 °C)/BrA1 | 0.51 | 0.55 | 40 | 0.11 |

($J_{sc}$ = 0.63 mA/$cm^2$) is higher than those of other $TiO_2$NR/BrA1-based photoanodes. The $J_{sc}$ values for $TiO_2$NR (300 °C)/BrA1, $TiO_2$NR (400 °C)/BrA1, $TiO_2$NR (500 °C)/BrA1, and $TiO_2$NR (600 °C)/BrA1 are 0.48, 0.60, 0.63, and 0.55 mA/$cm^2$, respectively. On the other hand, the corresponding $V_{oc}$ values of the photoelectrodes are 0.50, 0.55, 0.52, and 0.51 V, respectively. The FF values of the photoelectrodes are 44, 48, 46, and 40, respectively, and the corresponding $\eta$ values of the photoelectrodes are 0.10, 0.16, 0.15, and 0.11%, respectively. Among the studied DSSCs, the $TiO_2$NR (400 °C)/BrA1 photoelectrode-based DSSC exhibited a higher photovoltaic performance than other photoelectrodes. This is due to effective light absorption and efficient charge generation and separation. Also, in this investigation, the calculated $V_{oc}$ and FF values for the $TiO_2$NR (400 °C)/BrA1 photoelectrode are higher than those of other photo-


https://doi.org/10.1021/acsomega.2c03208
ACS Omega 2022, 7, 35595−35609

electrodes ($TiO_2$NR (300 °C)/BrA1, $TiO_2$NR (500 °C)/BrA1, $TiO_2$NR (600 °C)/BrA1); for this reason, the photovoltaic performance of $TiO_2$NR (400 °C) is higher than that of other photoelectrodes. Finally, the $TiO_2$NR (400 °C)/BrA1 photoelectrodes exhibited a power conversion efficiency (PEC) of 0.16%.

**3.9. Electrochemical Impedance Spectroscopy (EIS) Analysis of $TiO_2$NR (300 °C)/BrA1, $TiO_2$NR (400 °C)/BrA1, $TiO_2$NR (500 °C)/BrA1, and $TiO_2$NR (600 °C)/BrA1 Photoanodes.** Electrochemical impedance spectroscopy (EIS) was used to investigate the charge transport properties and recombination of electrons in $TiO_2$NR/BrA1-based DSSCs. The EIS plots of the $TiO_2$NR (300 °C)/BrA1, $TiO_2$NR (400 °C)/BrA1, $TiO_2$NR (500 °C)/BrA1, and $TiO_2$NR (600 °C)/BrA1-based DSSCs under dark conditions and fitted by ZView software are shown in Figure 11. The inset shows the equivalent circuit used to fit the Nyquist plot of the $TiO_2$NR/BrA1-based DSSCs. EIS analysis was carried out to determine the effect of annealing temperature on the charge transfer resistance of $TiO_2$. The equivalent circuit consists of three resistance values and two capacitances. $R_s$ denotes the resistance between the FTO and $TiO_2$NR interface. The $R_s$ values are summarized in Table 4; the $TiO_2$NR (400 °C) photoanode shows 51.5 Ω resistance. In contrast, $R_1$ and $R_2$ are the bulk charge transfer and charge transport resistance ($R_2$) between the $TiO_2$NR-based photoelectrodes and the electrolyte interface. CPE1 is the double-layer capacitance corresponding to $R_1$, and CPE2 is the double-layer capacitance between the $TiO_2$NR photoelectrodes and the electrolyte interface.[70,101,102] The charge transfer resistance $R_2$ at the FTO-$TiO_2$ and electrolyte interfaces is very high in the as-grown photoanode, suggesting that it contains many defects and impurities. Further, as shown in Table 4, at 400 °C annealing temperature, the $R_2$ value drastically decreases from 11 979 to 4445 Ω, indicating the reduced grain boundary defects at the interface and enhancement of the charge transport efficiency in $TiO_2$ nanorods. However, FTO annealed at 500 and 600 °C showed high resistance; as Sn diffusion starts at that annealing temperature, the increased resistance of the FTO, as well as the random nature of the $TiO_2$NRs in $TiO_2$NR (500 °C)/BrA1 and $TiO_2$NR (600 °C)/BrA1 photoanodes introduce several boundary resistances at both the interfaces.[79,103] This unexpected behavior might be explained using the packing density of the photoanodes, as shown in the FE-SEM cross-sectional view in Figure 3. The electron transport-recombination properties of the BrA1-sensitized $TiO_2$NR-based DSSCs are calculated from the equivalent circuit, Nyquist plot, and Bode plot and are represented in Table 4. It was reported that a decrease in the charge recombination rate resulted in an enhancement in device efficiency.[104] Figure S5 in ESI † shows the Bode phase plot, which is used to calculate the electron lifetime ($\tau_{eff}$) in DSSC[101] using the formula

$$\tau_{eff} = \frac{1}{2\pi f} \quad (5)$$

where $f$ is the maximum peak frequency of the semicircle; the calculated electron lifetime values of the $TiO_2$NR-based DSSCs are summarized in Table 4.

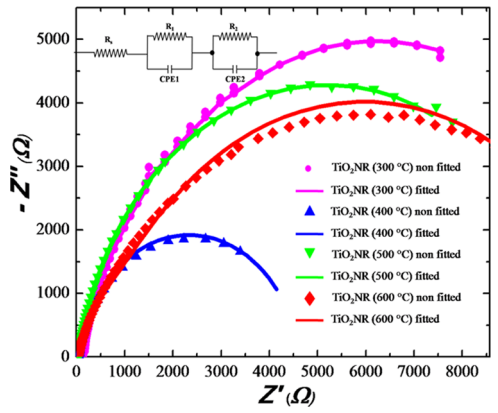


**Figure 11.** Nyquist plots of different annealed photoanodes of the DSSCs; the inset shows the equivalent circuit diagram used for EIS fitting.

## 4. CONCLUSIONS

2-Bromo-3-(methylamino)naphthalene-1,4-dione (BrA1) has been successfully synthesized using 2,3-dichloronaphthalene-1,4-dione. The as-synthesized BrA1 presents the centrosymmetric triclinic space group $P\bar{1}$, and the polymeric chains of asymmetric molecules of BrA1 have been systematically presented using the ORTEP diagram. Further, the synthesized dye was loaded on hydrothermally prepared $TiO_2$NR photoanodes annealed at different temperatures. The powder XRD confirms the rutile $TiO_2$NR's tetragonal phase, and with an increase in calcination temperature of the photoanodes, the average crystallite size increases from 37.69 to 41.57 nm. The SEM micrographs confirm the improved interface contact between the $TiO_2$NR and substrate, increasing the calcination temperature. The presence of Ti 2p, Ti 2s, and O 1s XPS peaks at binding energies of 458.4, 565.4, and 529.4 confirms the formation of $TiO_2$NR. The red shift in the absorption edge is observed in the BrA1-loaded $TiO_2$NR as the calcination temperature advances. Optimum $TiO_2$ nanorods annealed at 400 °C temperature loaded with the optimum photosensitizer were used as photoanodes to fabricate the DSSCs. It was further observed that on increasing the calcination, $TiO_2$NR-based DSSC cells ((400 °C)/BrA1, $TiO_2$NR (500 °C)/BrA1, and $TiO_2$NR (600 °C)/BrA1) exhibited significantly increased electron lifetimes than $TiO_2$NR (300 °C)/BrA1.

**Table 4. Electron Transport Properties of the BrA1-sensitized $TiO_2$NR-based DSSCs**

| samples/DSSC parameters | $R_s$ (Ω) | $R_1$ (Ω) | $R_2$ (Ω) | $R_2/R_1$ | frequency (Hz) | $\tau_{eff}$ (m s) | $L_n$ | $\tau_D$ (m s) | $D_{eff}$ (m $s^{-1}$) | $L_{eff}$ (mm) |
|---|---|---|---|---|---|---|---|---|---|---|
| $TiO_2$NR (300 °C)/BrA1 | 51.5 | 47 | 11 979 | 249 | 2454 | 0.06 | 15 | 0.0002 | 8.49 | 0.7371 |
| $TiO_2$NR (400 °C)/BrA1 | 51.7 | 161 | 4445 | 27 | 354 | 0.44 | 5 | 0.0159 | 0.1465 | 0.2538 |
| $TiO_2$NR (500 °C)/BrA1 | 51.5 | 17 | 10 290 | 577 | 602 | 0.26 | 24 | 0.0004 | 3.30 | 0.9262 |
| $TiO_2$NR (600 °C)/BrA1 | 51.9 | 52 | 10 803 | 207 | 794 | 0.20 | 14 | 0.0096 | 3.53 | 0.8402 |



https://doi.org/10.1021/acsomega.2c03208
ACS Omega 2022, 7, 35595−35609

## ■ ASSOCIATED CONTENT

### Supporting Information

The Supporting Information is available free of charge at https://pubs.acs.org/doi/10.1021/acsomega.2c03208.

Crystallographic data (CIF)

The images of bond distances of BrA1 photosensitizer (Figure S1), neighboring molecule of the asymmetric unit of BrA1(Figure S2), full width half-maximum (FWHM) of 101 peak of $TiO_2$NR electrodes annealed at 300, 400, 500 and 600 °C (Figure S3), $J-V$ curves of the DSSC device prepared using $TiO_2$NR (400 °C) without the photosensitizer (Figure S4), bode phase plot of $TiO_2$NR electrodes annealed at 300, 400, 500, and 600 °C (Figure S5), respectively. The crystallographic data for BrA1 can be shown in Tables S1−S7 (PDF)

### Accession Codes

The crystallographic data have been deposited with the Cambridge Crystallographic Data Centre (CCDC). They may be obtained on request by quoting the CCDC deposition number 2095627 from CCDC, 12 Union Road, Cambridge CB21EZ, UK (fax: +44 1223 336 033; E-mail address: deposit@ccdc.cam.ac.UK).

## ■ AUTHOR INFORMATION


### Corresponding Authors

**Habib M. Pathan** − *Advanced Physics Laboratory, Department of Physics, Savitribai Phule Pune University, Pune 411007, India*; Email: pathan@physics.unipune.ac.in

**Sunita Salunke-Gawali** − *Department of Chemistry, Savitribai Phule Pune University, Pune 411007, India*; orcid.org/0000-0002-4460-3992; Email: sunita.salunke@unipune.ac.in

### Authors

**Sharad A. Mahadik** − *Department of Chemistry, Savitribai Phule Pune University, Pune 411007, India; Advanced Physics Laboratory, Department of Physics, Savitribai Phule Pune University, Pune 411007, India*

**Ray J. Butcher** − *Department of Chemistry, Howard University, Washington, District of Columbia 20059, United States*

Complete contact information is available at: https://pubs.acs.org/10.1021/acsomega.2c03208


### Notes

The authors declare no competing financial interest.

## ■ ACKNOWLEDGMENTS

HMP and SSG are grateful to the Solar Energy Research and Development (SERD) Department of Science and Technology (DST), Government of India, for financial support through the Major Research project vide Sanction order DST/TMD/CERI/RES/2020/47 (G). SAM is thankful to Chhatrapati Shahu Maharaj Research, Training and Human Development Institute Pune, India, for financial support through the Vide Chhatrapati Shahu Maharaj Research Fellowship-2020 (CSMNRF-2020).

## ■ REFERENCES


(1) Takata, T.; Jiang, J.; Sakata, Y.; Nakabayashi, M.; Shibata, N.; Nandal, V.; Seki, K.; Hisatomi, T.; Domen, K. Photovoltaic water splitting with a quantum efficiency of almost unity. *Nature* **2020**, *581*, 411−414.

(2) Chen, S.; Takata, T.; Domen, K. Particulate photocatalysts for overall water splitting. *Nat. Rev. Mater.* **2017**, *2*, 17050.

(3) Sayyed, S. A.; Beedri, N. I.; Bhujbal, P. K.; Shaikh, S. F.; Pathan, H. M. Eosin-Y Sensitized Bi-layered ZnO Nanoflower-$CeO_2$ Photoanode for Dye-Sensitized Solar Cells Application. *ES Mater. Manuf.* **2020**, *10*, 45−51.

(4) Wu, W. Q.; Chen, D.; Caruso, R. A.; Cheng, Y. B. Recent progress in hybrid perovskite solar cells based on n-type materials. *J. Mate. Chem. A* **2017**, *5*, 10092−10109.

(5) Pawar, K. S.; Baviskar, P. K.; Inamuddin; Nadaf, A. B.; Salunke-Gawali, S.; Pathan, H. M. Layer-by-layer deposition of $TiO_2$−$ZrO_2$ electrode sensitized with Pandan leaves: natural dye-sensitized solar cell. *Mater. Renewable Sustainable Energy* **2019**, *8*, 12.

(6) Khadtare, S.; Bansode, A. S.; Mathe, V. L.; Shrestha, N. K.; Bathula, C.; Han, S. H.; Pathan, H. M. Effect of oxygen plasma treatment on performance of ZnO based dye sensitized solar cells. *J. Alloys Compd.* **2017**, *724*, 348−352.

(7) Rajendra Prasad, M. B.; Tamboli, P. S.; Bhalekar, V. P.; Kadam, V. S.; Abraham, J. T.; Rajesh, C.; Pathan, H. M. Impact of composition of polysulphide electrolyte on the photovoltaic performance in quantum dot sensitized solar cells. *Mater. Res. Express* **2018**, *5*, No. 066208.

(8) Wu, W. Q.; Xu, Y. F.; Liao, J. F.; Wang, L.; Kuang, D. B. Branched titania nanostructures for efficient energy conversion and storage: A review on design strategies, structural merits and multifunctionalities. *Nano Energy* **2019**, *62*, 791−809.

(9) Beedri, N. I.; Sayyed, SAAR.; Jadkar, S.; Pathan, H. M. *Rose Bengal Sensitized Niobium Pentaoxide Photoanode for Dye Sensitized Solar Cell Application*, AIP Conference Proceedings, 2017; p040022.

(10) Low, J.; Yu, J.; Jaroniec, M.; Wageh, S.; Al-Ghamdi, A. A. Heterojunction Photocatalysts. *Adv. Mater.* **2017**, *29*, No. 1601694.

(11) Xiao, M.; Wang, Z.; Lyu, M.; Luo, B.; Wang, S.; Liu, G.; Cheng, H.; Wang, L. Hollow Nanostructures for Photocatalysis: Advantages and Challenges. *Adv. Mater.* **2019**, *31*, No. 1801369.

(12) Kulkarni, A. N.; Rajendra Prasad, M. B.; Pathan, H. M.; Patil, R. S. $TiO_2$ photoanode sensitized with nanocrystalline $Bi_2S_3$: the effect of sensitization time and annealing on its photovoltaic performance. *Appl. Nanosci.* **2016**, *6*, 567−574.

(13) Beedri, N. I.; Baviskar, P. K.; Supekar, A. T.; Inamuddin; Jadkar, S. R.; Pathan, H. M. Bilayered ZnO/$Nb_2O_5$ photoanode for dye sensitized solar cell. *Int. J. Mod. Phys. B* **2018**, *32*, No. 1840046.

(14) Parveen, F.; Sannakki, B.; Jagtap, C. V.; Kadam, V. S.; Pathan, H. M. *Surface Plasmon Enhanced Performance of TiO2 Photoanode for Dye Sensitized Solar Cell Using Silver Nanoparticles*, AIP Conference Proceedings, 2018; p 030015.

(15) Arote, S.; Rajendra, Prasad. M. B.; Tabhane, V.; Pathan, H. M. Influence of geometrical thickness of $SnO_2$ based photoanode on the performance of Eosin-Y dye sensitized solar cell. *Opt. Mater.* **2015**, *49*, 213−217.

(16) Kulkarnia, A.; Grote, S.; Tabhane, V.; Pathan, H.; Patil, R. Photovoltaic Properties of $Bi_2Se_3$ Sensitized $SnO_2$ Photoanode Based Semiconductor Sensitized Solar Cell. *Adv. Sci. Lett.* **2016**, *22*, 876−879.

(17) Meng, A.; Zhang, L.; Cheng, B.; Yu, J. Dual Cocatalysts in $TiO_2$ Photocatalysis. *Adv. Mater.* **2019**, *31*, No. 1807660.

(18) Li, W.; Elzatahry, A.; Aldhayan, D.; Zhao, D. Core-shell structured titanium dioxide nanomaterials for solar energy utilization. *Chem. Soc. Rev.* **2018**, *47*, 8203−8237.

(19) Zhang, W.; He, H.; Li, H.; Duan, L.; Zu, L.; Zhai, Y.; Li, W.; Wang, L.; Fu, H.; Zhao, D. Visible-Light Responsive $TiO_2$-Based Materials for Efficient Solar Energy Utilization. *Adv. Energy Mater.* **2021**, *11*, No. 2003303.

(20) Zhang, W.; Tian, Y.; He, H.; Xu, L.; Li, W.; Zhao, D. Recent Advances in Synthesis of Hierarchically Mesoporous $TiO_2$ Materials for Energy and Environmental Applications. *Natl. Sci. Rev.* **2020**, *7*, 1702−1725.

(21) Wu, W.-Q.; Xu, Y.; Liao, J.; Wang, L.; Kuang, D. Branched titania nanostructures for efficient energy conversion and storage: A review on design strategies, structural merits and multifunctionalities. *Nano Energy* **2019**, *62*, 791−809.
(22) González-Verjan, V. A.; Trujillo-Navarrete, B.; Félix-Navarro, R. M.; Díaz de León, J. N.; Romo-Herrera, J. M.; Calva-Yáñez, J. C.; Hernández-Lizalde, J. M.; Reynoso-Soto, E. A. Effect of $TiO_2$ particle and pore size on DSSC efficiency. *Mater. Renewable Sustainable Energy* **2020**, *9*, 13.
(23) Zhao, D.; Peng, T.; Lu, L.; Cai, P.; Jiang, P.; Bian, Z. Effect of annealing temperature on the photoelectrochemical properties of dye-sensitized solar cells made with mesoporous $TiO_2$ nanoparticles. *J. Phys. Chem. C.* **2008**, *112*, 8486−8494.
(24) Liau, L.-K.; Wei-Wen, D. Process optimization of preparing spherical titania colloids with uniform distribution using artificial neural networks. *Colloids Surf., A* **2008**, *320*, 68−73.
(25) Calatayud, D.-G.; Rodríguez, M.; Jardiel, T. Controlling the morphology of $TiO_2$ nanocrystals with different capping agents. *Bol. Esp. Cer. Vid.* **2015**, *54*, 159−165.
(26) Li, X.-L.; Peng, Q.; Yi, J.-X.; Wang, X.; Li, Y.-D. Near monodisperse $TiO_2$ nanoparticles and nanorods. *Chem. Eur. J.* **2006**, *12*, 2383.
(27) Zhang, H.; Zhang, H.; Zhu, P.; Huang, F. Morphological effect in photocatalytic degradation of direct blue over mesoporous $TiO_2$ catalysts. *Chemistry Select* **2017**, *2*, 3282−3288.
(28) Mathew, S.; Yella, A.; Gao, P.; Humphry-Baker, R.; Curchod, BFE.; Ashari-Astani, N.; Tavernelli, I.; Rothlisberger, U.; Nazeeruddin, M. K.; Grätzel, M. Dye-sensitized solar cells with 13% efficiency achieved through the molecular engineering of porphyrin sensitizers. *Nat. Chem.* **2014**, *6*, 242−247.
(29) Kakiage, K.; Aoyama, Y.; Yano, T.; Oya, K.; Fujisawa, J.; Hanaya, M. Highly-efficient dye-sensitized solar cells with collaborative sensitization by silyl-anchor and carboxy-anchor dyes. *Chem. Commun.* **2015**, *51*, 15894−15897.
(30) Chava, R. K.; Lee, W. M.; Oha, S. Y.; Jeong, K. U.; Yu, Y. T. Improvement in light-harvesting and device performance of dye sensitized solar cells using electrophoretic deposited hollow $TiO_2$NPs scattering layer. *Sol. Energy Mater. Sol. Cells* **2017**, *161*, 255−262.
(31) Wu, J.; Lan, Z.; Lin, J.; Huang, M.; Huang, Y.; Fan, L.; Luo, G. Electrolytes in dye sensitized solar cells. *Chem. Rev.* **2015**, *115*, 2136−2173.
(32) Thomas, S.; Deepak, T.; Anjusree, G.; Arun, T.; Nair, S. V.; Nair, A. S. A review on counter electrode materials in dye-sensitized solar cells. *J. Mater. Chem. A* **2014**, *2*, 4474−4490.
(33) Hart, A. S.; Chandra, BKC.; Subbaiyan, N. K.; Karr, P. A.; D'Souza, F. Phenothiazine sensitized organic solar cells: effect of dye anchor group positioning on the cell performance. *ACS. Appl. Mater. Interfaces* **2012**, *4*, 5813−5820.
(34) Hagfeldt, A.; Boschloo, G.; Sun, L.; Kloo, L.; Pettersson, H. Dye-sensitized solar cells. *Chem. Rev.* **2010**, *110*, 6595−6663.
(35) Sayama, K.; Sugihara, H.; Arakawa, H. Photoelectrochemical Properties of a Porous $Nb_2O_5$ Electrode Sensitized by a Ruthenium Dye. *Chem. Mater.* **1998**, *10*, 3825−3832.
(36) Keis, K.; Magnusson, E.; Lindstrom, H.; Lindquist, S. E.; Hagfeldt, A. A 5% Efficient Photo Electrochemical Solar Cell Based on Nanostructured ZnO Electrodes. *Sol. Energy Mater Sol. Cells* **2002**, *73*, 51−58.
(37) Mahadik, S. A.; Pathan, H. M.; Salunke-Gawali, S.; Butcher, R. J. Aminonaphthoquinones as photosensitizers for mesoporous ZnO based dye-sensitized solar cells. *J. Alloys. Compd.* **2020**, *845*, No. 156279.
(38) Wu, W. Q.; Xu, Y. F.; Su, C. Y.; Kuang, D. B. Ultra-long anatase $TiO_2$ nanowire arrays with multi-layered configuration on FTO glass for high-efficiency dye-sensitized solar cells. *Energy Environ. Sci.* **2014**, *7*, 644−649.
(39) Sharma, K.; Sharma, V.; Sharma, S. S. Dye-Sensitized Solar Cells: Fundamentals and Current Status. *Nanoscale Res. Lett.* **2018**, *13*, 381.
(40) Tsubomura, H.; Matsumura, M.; Nomura, Y.; Amamiya, T. Dye sensitized zinc oxide: aqueous electrolyte: platinum photocell. *Nature* **1976**, *261*, 402−403.
(41) O'Regan, B.; Grätzel, M. A low-cost, high-efficiency solar cell based on dye-sensitized colloidal $TiO_2$ films. *Nature* **1991**, *353*, 737−740.
(42) Nazeeruddin, M. K.; Baranoff, E.; Gratzel, M. Dye-sensitized solar cells: A brief overview. *Sol. Energy* **2011**, *85*, 1172−1178.
(43) Altobello, S.; Bignozzi, C. A.; Caramori, S.; Larramona, G.; Quici, S.; Marzanni, G.; Lakhmiri, R. Sensitization of $TiO_2$ with ruthenium complexes containing boronic acid functions. *J. Photochem. Photobiol., A* **2004**, *166*, 91−98.
(44) Kakiage, K.; Aoyama, Y.; Yano, T.; Oya, K.; Fujisawab, J.; Hanaya, M. Highly-efficient dye-sensitized solar cells with collaborative sensitization by silyl-anchor and carboxy-anchor dyes. *Chem. Commun.* **2015**, *51*, 15894−15897.
(45) Sayama, K.; Sugihara, H.; Arakawa, H. Photoelectrochemical Properties of a Porous $Nb_2O_5$ Electrode Sensitized by a Ruthenium Dye. *Chem. Mater.* **1998**, *10*, 3825−3832.
(46) Lin, Y.-J.; Chen, J.-W.; Hsiao, P.-T.; Tung, Y.-L.; Chang, C.-C.; Chen, C.-M. Efficiency improvement of dye-sensitized solar cells by in situ fluorescence resonance energy transfer. *J. Mater. Chem. A* **2017**, *5*, 9081−9089.
(47) Kurumisawa, Y.; Higashino, T.; Nimura, S.; Tsuji, Y.; Iiyama, H.; Imahori, H. Renaissance of Fused Porphyrins: Substituted Methylene-Bridged Thiophene-Fused Strategy for High-Performance Dye-Sensitized Solar Cells. *J. Am. Chem. Soc.* **2019**, *141*, 9910−9919.
(48) Hwang, S.; Lee, J. H.; Park, C.; Lee, H.; Kim, C.; Park, C.; Lee, M.-H.; Lee, W.; Park, J.; Kim, K.; Park, N.-G.; Kim, C. A highly efficient organic sensitizer for dye-sensitized solar cells. *Chem. Commun.* **2007**, 4887−4889.
(49) Nguyen, W. H.; Bailie, C. D.; Burschka, J.; Moehl, T.; Grätzel, M.; McGehee, M. D.; Sellinger, A. Molecular Engineering of Organic Dyes for Improved Recombination Lifetime in Solid-State Dye-Sensitized Solar Cells. *Chem. Mater.* **2013**, *25*, 1519−1525.
(50) Sil, M. C.; Sudhakar, V.; Mele Kavungathodi, M. F.; Punitharasu, V.; Nithyanandhan, J. Orthogonally Functionalized Donor/Acceptor Homo- and Heterodimeric Dyes for Dye-Sensitized Solar Cells: An Approach to Introduce Panchromaticity and Control the Charge Recombination. *ACS. Appl. Mater. Interfaces* **2017**, *9*, 34875−34890.
(51) Nazeeruddin, M. K.; Pe'chy, P.; Renouard, T.; Zakeeruddin, S. M.; Baker, R. H.; Comte, P.; Liska, P.; Cevey, L.; Costa, E.; et al. Engineering of efficient panchromatic sensitizers for nanocrystalline $TiO_2$-based solar cells. *J. Am. Chem. Soc.* **2001**, *123*, 1613−1624.
(52) Salunke-Gawali, S.; Pawar, O.; Nikalje, M.; Patil, R.; Weyhermüller, T.; Puranik, V. G.; Konkimalla, V. B. Synthesis, characterization and molecular structures of homologated analogs of 2-bromo-3-(n-alkylamino)-1,4-naphthoquinone. *J. Mol. Struct.* **2014**, *1056-1057*, 97−103.
(53) Perrin, D. D.; Armarego, W.; Perrin, D. R. *Pergamon Press London* **1988**, 260.
(54) Burfield, D. R.; Smithers, R. H. Desiccant efficiency insolvent and reagent drying. 7. Alcohols. *J. Org. Chem.* **1983**, *48*, 2420−2422.
(55) Khadtare, S. S.; Ware, A. P.; Salunke−Gawali, S.; Jadkar, S. R.; Pingale, S. S.; Pathan, H. M. Dye Sensitized Solar Cell with Lawsone Dye Using ZnO Photoanode: Experimental and TD-DFT Study. *RSC Adv.* **2015**, *5*, 17647−17652.
(56) Khadtare, S. S.; Jadkar, S. R.; Salunke−Gawali, S.; Pathan, H. M. Lawsone Sensitized ZnO Photoelectrodes for Dye Sensitized Solar Cells. *J. Nano. Res.* **2013**, *24*, 140−145.
(57) Mahadik, M. A.; Shinde, P. S.; Cho, M.; Jang, J. S. Fabrication of a ternary $CdS/ZnIn_2S_4/TiO_2$ heterojunction for enhancing photoelectrochemical performance: effect of cascading electron-hole transfer. *J. Mater. Chem. A* **2015**, *3*, 23597−23606.
(58) David, S.; Mahadik, M. A.; Chung, H.; Ryu, J. H.; Jang, J. S. Facil Hydrothermally Synthesized a Novel CdS Nano flower/Rutile-$TiO_2$ Nanorod Heterojunction Photoanode Used for Photoelectro-


https://doi.org/10.1021/acsomega.2c03208
*ACS Omega* 2022, 7, 35595−35609

catalytic Hydrogen Generation. *ACS. Sustain. Chem. Eng.* **2017**, *5*, 7537−7548.
(59) An, G. W.; Mahadik, M. A.; Chae, W. S.; Kim, H. G.; Cho, M.; Jang, J. S. Enhanced Solar Photoelectrochemical Conversion Efficiency of the Hydrothermally-deposited $TiO_2$ Nanorod Arrays: Effects of the Light Trapping and Optimum Charge Transfer. *Appl. Surf. Sci.* **2018**, *440*, 688−699.
(60) Mahadik, M. A.; Shinde, P. S.; Cho, M.; Jang, J. S. Metal oxide top layer as an interfacial promoter on a $ZnIn_2S_4/TiO_2$ heterostructure photoanode for enhanced photoelectrochemical performance. *Appl. Catal.* **2016**, *184*, 337−346.
(61) Aydil, E. S.; Liu, B. J. Growth of Oriented Single-Crystalline Rutile $TiO_2$ Nanorods on Transparent Conducting Substrates for Dye-Sensitized Solar Cells. *J. Am. Chem. Soc.* **2009**, *131*, 3985−3990.
(62) *Bruker, APEX2, SAINT, SADABS*; Bruker AXS Inc.: Madison, Wisconsin, USA, 2007.
(63) Macrae, C. F.; Bruno, I. J.; Chisholm, J. A.; Edgington, P. R.; Mc Cabe, P.; Pidcock, E.; Rodriguez-Monge, L.; Taylor, R.; van de Streek, J.; Wood, P. A. Mercury CSD 2.0 − new features for the visualization and investigation of crystal structures. *J. Appl. Crystallogr.* **2008**, *41*, 466−470.
(64) Sheldrick, G. M. A short history of SHELX. *Acta. Crystallogr. A* **2008**, *64*, 112−122.
(65) Spek, A. L. Structure validation in chemical crystallography. *Acta. Crystallogr. D* **2009**, *65*, 148−155.
(66) Agarwal, G.; Lande, D. N.; Chakravarty, D.; Gejji, S. P.; Gosavi-Mirkute, P.; Patil, A.; Salunke-Gawali, S. Bromine substituted aminonaphthoquinones: synthesis, characterization, DFT, and metal ion binding studies. *RSC. Adv* **2016**, *6*, 88010−88029.
(67) Dar, U. A.; Bhand, S.; Lande, D. N.; Rao, S. S.; Patil, Y. P.; Gejji, S. P.; Nethaji, M.; Weyhermüller, T.; Salunke-Gawali, S. Molecular structures of 2-hydroxy-1,4-naphthoquinone derivatives and their zinc(II) complexes: Combining experiment and density functional theory. *Polyhedron* **2016**, *113*, 61−72.
(68) Choudhari, D.; Chakravarty, D.; Lande, D. N.; Parveen, S.; Gejji, S. P.; Kodam, K. M.; Salunke-Gawali, S. Crystal structures and biological activity of homologated (N) -*n*-alkylammonium salts of 2-bromo-3-oxido-1,4-naphthoquinone. *J. Struct. Chem.* **2019**, *30*, 2257−2270.
(69) Salunke-Gawali, S.; Pereira, E.; Dar, U. A.; Bhand, S. Metal complexes of hydroxynaphthoquinones: Lawsone, bis-lawsone, lapachol, plumbagin and juglone. *J. Mol. Struc.* **2017**, *1148*, 435.
(70) Mahadik, S. A.; Patil, A.; Pathan, H. M.; Salunke-Gawali, S.; Butcher, R. J. Thionaphthoquinones as Photosensitizers for $TiO_2$ Nanorods and ZnO Nanograin Based Dye-sensitized Solar Cells: Effect of Nanostructures on Charge Transport and Photovoltaic Performance. *Eng. Sci.* **2021**, *14*, 46−58.
(71) Ghicov, A.; Tsuchiya, H.; Macak, J. M.; Schmuki, P. Annealing effects on the photoresponse of $TiO_2$ nanotubes. *Phys. Status Solidi A* **2006**, *203*, R28−R30.
(72) Wu, J.; Lu, H.; Zhang, X.; Raziq, F.; Qu, Y.; Jing, L. Enhanced charge separation of rutile $TiO_2$ nanorods by trapping holes and transferring electrons for efficient cocatalyst-free photocatalytic conversion of $CO_2$ to fuels. *Chem. Commun.* **2016**, *52*, 5027−5029.
(73) Xie, Z.; Shuang, S.; Ma, L.; Zhu, F.; Liu, X.; Zhang, Z. Annealing effect on the photoelectrochemical and photocatalytic performance of $TiO_2$ nanorod arrays. *RSC. Adv.* **2017**, *7*, 51382−51390.
(74) Mathews, N. R.; Morales, E. R.; Cortés-Jacome, M. A.; Antonio, J. A. T. $TiO_2$ thin films − Influence of annealing temperature on structural, optical and photocatalytic properties. *Sol. Energy* **2009**, *83*, 1499−1508.
(75) Baviskar, P. K.; Tan, W.; Zhang, J.; Sankapal, B. R. Wet chemical synthesis of ZnO thin films and sensitization to light with N3 dye for a solar cell application. *J. Phys. D: Appl. Phys.* **2009**, *42*, No. 125108.
(76) Monshi, A.; Foroughi, M. R.; Monshi, M. R. Modified Scherrer Equation to Estimate More Accurately Nano-Crystallite Size Using XRD. *World J. Nano Sci. Eng.* **2012**, *2*, 154−160.
(77) Peng, T.; Zhao, D.; Dai, K.; Shi, W.; Hirao, K. Synthesis of Titanium Dioxide Nanoparticles with Mesoporous Anatase Wall and High Photocatalytic Activity. *J. Phys. Chem. B.* **2005**, *109*, 4947−4952.
(78) Zhao, D.; Peng, T.; Lu, L.; Cai, P.; Jiang, P.; Bian, Z. Effect of Annealing Temperature on the Photoelectrochemical Properties of Dye-Sensitized Solar Cells Made with Mesoporous $TiO_2$ Nanoparticles. *J. Phys. Chem. C* **2008**, *112*, 8486−8494.
(79) Mahadik, M. A.; Shinde, P. S.; Lee, H. H.; Cho, M.; Jang, J. S. Highly efficient and stable 3D $Ni(OH)_2/CdS/ZnIn_2S_4/TiO_2$ heterojunction under solar light: Effect of an improved $TiO_2$/FTO interface and cocatalyst. *Sol. Energy Mater. Sol. Cells* **2017**, *159*, 475−487.
(80) Zhou, J.; Ren, F.; Zhang, S.; Wu, W.; Xiao, X.; Liu, Y.; Jiang, C. $SiO_2$−Ag−$SiO_2$−$TiO_2$ multi-shell structures: plasmon enhanced photocatalysts with wide-spectral-response. *J. Mater. Chem. A* **2013**, *1*, 13128−13138.
(81) Ghazzal, M. N.; Chaoui, N.; Genet, M.; Gaigneaux, E. M.; Robert, D. Effect of compressive stress-inducing a bandgap narrowing on the photoinduced activities of sol-gel $TiO_2$ films. *Thin Solid Films* **2011**, *520*, 1147−1154.
(82) Nagaveni, K.; Hegde, M. S.; Ravishankar, N.; Subbanna, G. N.; Madras, G. Synthesis and Structure of Nanocrystalline $TiO_2$ with Lower Band Gap Showing High Photocatalytic Activity. *Langmuir.* **2004**, *20*, 2900−2907.
(83) Perpète, E. A.; Lambert, C.; Wathelet, V.; Preat, J.; Jacquemin, D. Ab initio studies of the $\lambda_{max}$ of naphthoquinones dyes. *Spectrochim. Acta, Part A* **2007**, *68*, 1326−1333.
(84) Patil, R.; Chadar, D.; Chaudhari, D.; Peter, J.; Nikalje, M.; Weyhermüller, T.; Salunke-Gawali, S. Synthesis and characterization of 2-(n-alkylamino)-1,4-naphthoquinone: Molecular structures of ethyl and hexyl derivatives. *J. Mol. Struct.* **2014**, *1075*, 345−351.
(85) Pawar, O.; Patekar, A.; Khan, A.; Kathawate, L.; Haram, S.; Markad, G.; Puranik, V.; Salunke-Gawali, S. Molecular structures and biological evaluation of 2-chloro-3- (n-alkylamino)-1,4-naphthoquinone derivatives as potent antifungal agents. *J. Mol. Struct.* **2014**, *1059*, 68−74.
(86) Zhang, J.; Zhou, P.; Liu, J.; Yu, J. New understanding of the difference of photocatalytic activity among anatase, rutile and brookite $TiO_2$. *Phys. Chem. Chem. Phys.* **2014**, *16*, 20382−20386.
(87) Kim, N. Y.; Lee, H. K.; Moon, J. T.; Joo, J. B. Synthesis of Spherical $TiO_2$ Particles with Disordered Rutile Surface for Photocatalytic Hydrogen Production. *Catalysts* **2019**, *9*, 491.
(88) Patil, R.; Bhand, S.; Konkimalla, V. B.; Banerjee, P.; Ugal, B.; Chadar, D.; Saha, S. K.; Praharaj, P. P.; Nagaraja, C. M.; Chakravarty, D.; Salunke-Gawali, S. Molecular association of 2-(n-alkylamino)-1,4-naphthoquinone derivatives: Electrochemical, DFT studies and Antiproliferative activity against leukemia cell lines. *J. Mol. Struct.* **2016**, *1125*, 272−281.
(89) Adeniyi, A. A.; Ngake, T. L.; Conradie, J. Cyclic Voltammetric Study of 2-Hydroxybenzophenone (HBP) Derivatives and the Correspondent Change in the Orbital Energy Levels in Different Solvents. *Electroanalysis* **2020**, *32*, 2659−2668.
(90) Vandewal, K.; Benduhn, J.; Nikolis, V. C. How to determine optical gaps and voltage losses in organic photovoltaic materials. *Sustainable Energy Fuels* **2018**, *2*, 538−544.
(91) Sahoo, S. S.; Salunke-Gawali, S.; Kadam, V. S.; Pathan, H. M. Canna Lily Red and Yellow Flower Extracts: A New Power Source to produce Photovoltage through Dye-Sensitized Solar Cells. *Energy Fuels* **2020**, *34*, 9674−9682.
(92) Ketterer, B.; Heiss, M.; Livrozet, M. J.; Rudolph, A.; Reiger, E.; Morral, A. F. determination of the bandgap and the split-off band in wurtzite GaAs using Raman and photoluminescence excitation spectroscopy. *Phys. Rev. B* **2011**, *83*, No. 125307.
(93) Adeniyi, A. A.; Ngake, T.; Conradie, J. Cyclic Voltammetric Study of 2-Hydroxybenzophenone (HBP) Derivatives and the Correspondent Change in the Orbital Energy Levels in Different Solvents. *Electroanalysis* **2020**, *32*, 2659−2668.


https://doi.org/10.1021/acsomega.2c03208
*ACS Omega* 2022, 7, 35595−35609

(94) Usami, A.; Seki, S.; Mita, Y.; Kobayashi, H.; Miyashiro, H.; Terada, N. Temperature dependence of open-circuit voltage in dye-sensitized solar cells. *Sol. Energy Mater. Sol. Cells* **2009**, *93*, 840−842.
(95) Wang, Y.; Muramatsu, A.; Sugimoto, T. FTIR analysis of well-defined $\alpha$-$Fe_2O_3$ particles. *Colloids Surf., A* **1998**, *134*, 281−297.
(96) Baviskar, P. K.; Zhang, J. B.; Gupta, V.; Chand, S.; Sankapal, B. R. Nanobeads of zinc oxide with rhodamine B dye as a sensitizer for dye-sensitized solar cell application. *J. Alloys Compd.* **2012**, *510*, 33−37.
(97) Borbón, S.; Lugo, S.; Pourjafari, D.; Aguilar, N. P.; Oskam, G.; López, I. Open-Circuit Voltage ($V_{OC}$) Enhancement in $TiO_2$-Based DSSCs: Incorporation of ZnO Nanoflowers and Au Nanoparticles. *ACS Omega* **2020**, *5*, 10977−10986.
(98) Fabregat-Santiago, F.; Germa, G. B.; Ivan, M. S.; Juan, B. Characterization of nanostructured hybrid and organic solar cells by impedance spectroscopy. *Phys. Chem. Chem. Phys.* **2011**, *13*, 9083−9118.
(99) Yan, H.; Wang, J.; Feng, B.; Duan, K.; Weng, J. Graphene and Ag nanowires co-modified photoanodes for high-efficiency dye-sensitized solar cells. *Sol. Energy* **2015**, *122*, 966−975.
(100) Jiang, Y.; Yang, Y.; Zhu, J.; Qiang, L.; Ye, T.; Li, L.; Sua, T.; Fan, R. Nickel silicotungstate-decorated Pt photocathode as an efficient catalyst for triiodide reduction in dye-sensitized solar cells. *Dalton Trans.* **2016**, *45*, 16859−16868.
(101) Beedri, N. I.; Baviskar, P. K.; Mahadik, M. A.; Jadkar, S. R.; Jang, J. S.; Pathan, H. M. Efficiency Enhancement for Cocktail Dye Sensitized $Nb_2O_5$ Photoanode Towards Dye Sensitized Solar Cell. *Eng. Sci.* **2019**, *8*, 76−82.
(102) Majumder, S.; Baviskar, P. K.; Sankapal, B. R. Light-induced electrochemical performance of 3D- CdS nanonetwork: Effect of annealing. *Electrochim. Acta* **2016**, *222*, 100−107.
(103) Jia, L.; Xie, J.; Guo, C.; Li, C. M. Modification of a thin layer of $\alpha$-$Fe_2O_3$ onto a largely voided $TiO_2$ nanorod array as a photoanode to significantly improve the photoelectrochemical performance toward water oxidation. *RSC Adv.* **2015**, *5*, 62611−62618.
(104) Seo, K. D.; You, B. S.; Choi, I. T.; Ju, M. J.; You, M.; Kang, H. S.; Kim, H. K. Dual-channel anchorable organic dyes with well-defined structures for highly efficient dye-sensitized solar cells. *J. Mater. Chem. A* **2013**, *1*, 9947−9953.


https://doi.org/10.1021/acsomega.2c03208
*ACS Omega* 2022, 7, 35595−35609